UNIVERSITY OF OKLAHOMA

GRADUATE COLLEGE

FAULT RUPTURE PROCESSES DURING HIGH VELOCITY ROTARY SHEAR EXPERIMENTS

A THESIS

SUBMITTED TO THE GRADUATE FACULTY

in partial fulfillment of the requirements for the

Degree of

MASTER OF SCIENCE

By

XIMENG ZU
Norman, Oklahoma
2016

FAULT RUPTURE PROCESSES DURING HIGH VELOCITY ROTARY SHEAR EXPERIMENTS

A THESIS APPROVED FOR THE
CONOCOPHILLIPS SCHOOL OF GEOLOGY AND GEOPHYSICS

BY

_____
Dr. Ze'ev Reches, Chair

_____
Dr. Xiaowei Chen

_____
Dr. Shankar Mitra

Acknowledgements

First and foremost, I would like to express my thanks to Dr. Ze'ev Reches for supporting me with his extensive knowledge and enlightening wit. Also, many thanks to Dr. Shankar Mitra and Dr. Xiaowei Chen for their advising and valuable comments. Thanks to Dr. Brett Carpenter for helping me on my research work and thesis writing with his professional knowledge and insightful advice. I would like to thank my friends Jianjun, Chance, Wen, Jefferson, Zonghu, Xiaofeng for sharing their knowledge and helping me with life and study. Their advice and suggestions were very helpful and beneficial to me. Last but not least, I would like to express my gratitude to Luyao and my parents for their affection and care for me during my pursuit to Master's degree.

The financial support for this research was provided by NSF-Geophysics award 1345087 "Experimental simulation of earthquake rupture processes", and by continuous support by ConocoPhillips and Anadarko Oil to my advisor, Dr. Ze'ev Reches.

Table of Contents

List of Tables

List of Figures

Abstract

High velocity shear experiments can provide information on fault rupture processes that seismological methods cannot. The present study focuses on two main aspects of fault rupture processes. One is developing a new, realistic, experimental loading method, power-density control, which can generate stick-slip motion, which is a laboratory model of earthquakes. This method uses energy-rate (power) loading instead of the classical velocity loading, and it generates multiple, spontaneous, high-velocity stick-slips. Our power-density experiments produced events that are comparable to natural earthquakes in terms of slip-velocity and slip displacement. The other aspect of the present research involves investigating acoustic emissions (AEs) recorded with 3D accelerometers during the shear experiments. With four accelerometers on the sample, I located the sources of AEs that are interpreted as asperity breakdown on the experimental fault surface. I conducted 66 velocity control experiments and 76 power-density control experiments on samples of granite, diorite, and limestone, at slip rates approaching seismic slip velocities (~ 1 m/s); 70 of the experiments with AE data. The combined results show that power-density control loading with AE recording has the potential to generate realistic simulations of fault rupture with rupture visualization.

Chapter 1 Introduction

Earthquake science

Large earthquakes pose a great threat to society as they cause fatalities, demolish buildings, disrupt transportation, and lead to vast financial loss. Despite major progress in seismic research during the past few decades, earthquakes remain poorly understood. The nonlinear nature and opacity of the deforming crust are the main difficulties facing earthquake scientists (Kanamori and Brodsky, 2004). New technologies have provided methods that aid in deciphering earthquake processes, including high-performance computing and dense recording networks. Earthquake processes are investigated by four disciplines – seismology, geodesy, geology, and rock mechanics. My research falls into the categories of seismology and rock mechanics.

Rock mechanics of faulting processes

Overview

The study of faulting and rock mechanics focuses on macroscopic phenomena of fault slip and rock deformation based on microscopic observations and laboratory-derived theories. This aspect is integral to earthquake study because it allows connecting natural phenomena to laboratory observations. For example, laboratory experiments and microscopic observations identified fault lubrication mechanisms as an explanation for the dynamic weakening the must occur during rapid fault slip (Di Toro et al., 2011; Reches and Lockner, 2010). Experimental methods also tested the weakness of San Andreas Fault (Zoback et al., 1987) revealed by samples from the active fault zone (Carpenter et al., 2011; Lockner et al., 2011).

In the experiments, it is usually possible to characterize the rocks' and faults' properties under controlled stress, temperature, fluid chemistry, and strain-rate

conditions (Chen et al., 2013; Di Toro et al., 2011; Reches and Lockner, 2010; Shimamoto and Tsutsumi, 1994) and to compare the results to natural earthquakes. The experiments are complementary to seismological methods in obtaining mechanical information, such as stress evolution, slip history, and fault dilation. Yet, there are still gaps between laboratory scales of centimeters and field scales of kilometers.

Since the 1960s, the stick-slip phenomena have been used as an analog of crustal earthquakes (Byerlee and Brace, 1968). In the 1970s, servo-controlled testing machines were introduced and subsequent development included high precision, double-direct-shear (Dieterich, 1978) and rotary-shear devices (Tullis and Weeks, 1987). These technologies allowed for detailed friction measurements. For example, (Di Toro et al., 2004) found that friction falls towards zero in quartz rock as slip-velocity approaches seismic rates. (Sone and Shimamoto, 2009) tested the behavior of experimental fault gouge during accelerating and decelerating earthquake slip and found that the evolution of friction during earthquake slip is composed of weakening, strengthening, and healing.

Static and dynamic friction

The basic friction models consider a static friction coefficient, μ_s, of the frictional interface at rest, and a kinetic friction coefficient, μ_k, when the frictional interface is in motion. If $\mu_k < \mu_s$, instability can occur. In a real, physical system, the static friction evolves into kinetic friction over a finite slip distance, D_c, which is required for the static friction to drop to steady–state level (Fig. 1.1). The slip distance, D_c, is called the 'critical slip distance', and is a key parameter in frictional sliding models.

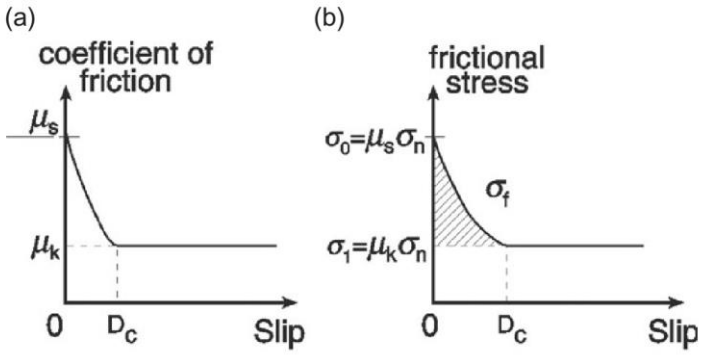

Fig. 1.1 Simple model of static and kinetic friction (Kanamori and Brodsky, 2004).

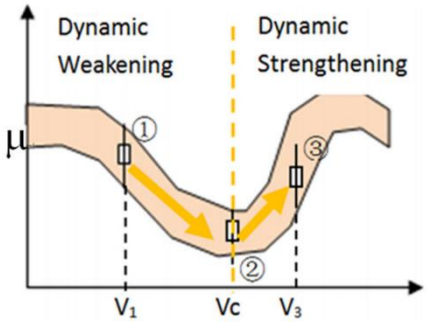

Fig. 1.2 Velocity dependence of friction (Liao and Reches, 2013). From v_1 to v_c, friction, μ, decreases with velocity (velocity weakening); from v_c to v_3, friction increases with velocity (velocity strengthening).

Velocity dependence of friction

Dynamic friction is the friction during slip and is a function of kinematic slip parameters such as slip-velocity. The friction dependence on velocity appears in two forms: velocity-strengthening when the friction increases as velocity increases, and velocity-weakening when friction decreases as velocity increases (Marone, 1998). It is shown for siliceous igneous rocks, the friction decreases with velocity from v_1 to v_c, whereas it increases from v_c to v_3 (Fig. 1.2). Velocity weakening and dynamic weakening, are necessary for the nucleation and propagation of a seismic event because it involves the positive feedback of acceleration and weakening that is necessary for slip instability.

Stick-slip experiments

In their landmark paper, Byerlee and Brace (1968) showed that a cylindrical, saw cut, rock sample loaded in a triaxial cell slips by a series of jerky motions. They suggested that, when confining pressures in the experiments achieved levels that prevail in the crust, the jerky motions, known as stick-slips, are proxies of crustal earthquakes (Fig. 1.3). Stick-slip behavior was later analyzed with biaxial systems in which two rock blocks are loaded until the two meter long experimental fault fails spontaneously while releasing the elastic energy stored in the rock blocks (Okubo and Dieterich, 1981). Lockner and Okubo (1983) showed that in these experiments, the fault strength (=measured shear stress) increased slightly during the initial stage, and then dropped abruptly while slipping to a distance of $d_c \cong 10$ μm (red curve in Fig. 1.4a). The fault continued to slip under quasi-uniform shear stress to a total distance of ~ 90 μm. The slip-velocity was jerky, including a few periods of slip direction inversion (blue curve in Fig. 1.4a). Ohnaka and Yamashita (1989) generated stick-slip events with ~ 4-μm displacement in a direct shear device (Fig. 1.4b). Here, the fault weakening (second curve from top, Fig. 1.4b) was similar to the equivalent in Lockner and Okubo (1983) (red curve in Fig. 1.4a). The velocity evolution shows a strong acceleration pulse, to the order of magnitude of km/s^2, followed by a steady deceleration (third curve from top, Fig. 1.4b). Karner and Marone (2000) found multiple and continuous jerky motions in biaxial shear experiments. They noted that at a given loading rate, there is a positive relation between stress drop and recurrence interval, and combined data from different velocities also show a positive relation between stress drop and recurrence interval. Their data showed stress drop and post-stick-slip stress levels depend on loading rate and recurrence interval in a complex way.

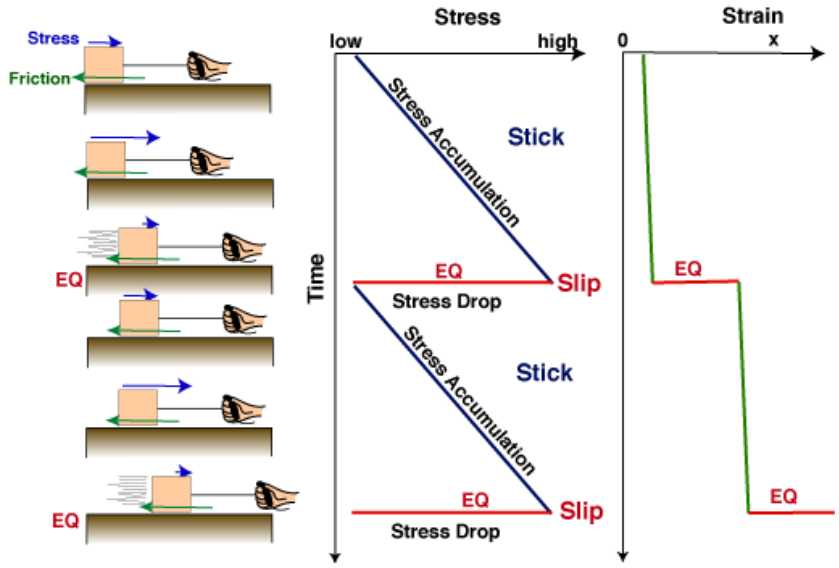

Fig. 1.3 Illustration of stick-slip and earthquakes. Left panel shows the mechanical process of a stick-slip with slider model. Middle panel shows the evolution of shear stress with time corresponding to the mechanical model to the left. Right panel show the evolution of shear strain during the process. This figure illustrates the similarities of stick-slip and earthquakes, justifying stick-slip as a good analog of earthquakes. (Lectures, Laske).

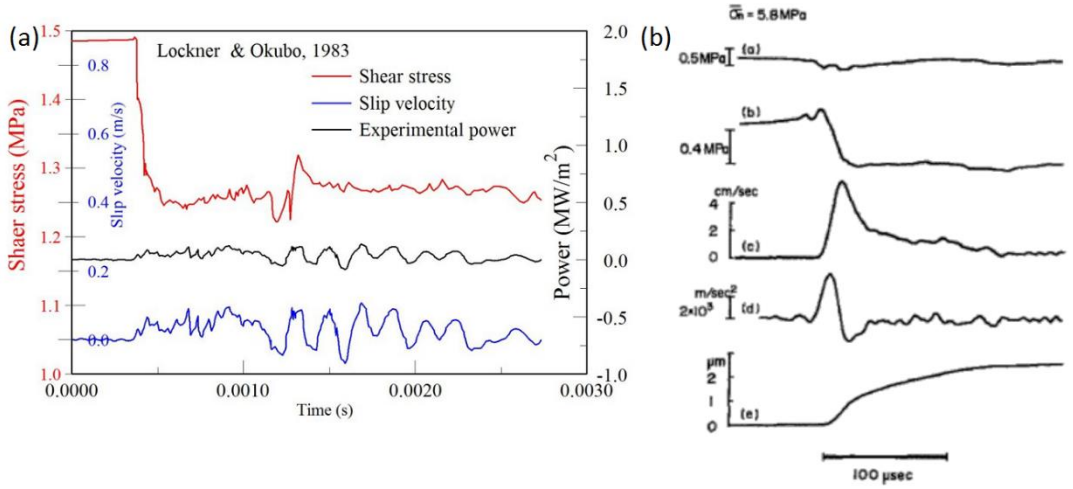

Fig. 1.4 Experimental stick-slip phenomena (Lockner and Okubo, 1983a; Ohnaka and Yamashita, 1989). See text for details.

Stick-slip experiments are analogous to earthquakes in terms of loading: in both cases, a finite amount of elastic energy is stored in the surrounding rocks, and experimental load frame, and the slip event spontaneously develops a history of fault

weakening and slip evolution (Beeler et al., 2001; Nielsen et al., 2010). However, due to practical limitations, experimental stick-slips are restricted to very small slip distances of a few tens of microns that are 5-6 orders of magnitude less than large earthquake displacements. These slip events may simulate earthquake nucleation, but fall short of the mechanical power (Di Toro et al., 2011) and slip magnitude of larger earthquakes.

High-speed, rotary shear experiments

Rotary shear experiments on cylindrical rock samples allow for high velocity, a few m/s, and unlimited slip distances, a significant advantage relative to the short displacement of direct shear and triaxial experiments (Shimamoto and Tsutsumi, 1994). The most commonly used experimental loading mode is controlled-velocity in which the slip-velocity history is predetermined and controlled by the controlling system. The slip-velocity history may be a constant velocity throughout the experiment, or stepping values including acceleration and deceleration. For example, Sone and Shimamoto (2009) applied the velocity history determined by slip inversion of the 1999 Chi-Chi earthquake. Chang et al. (2012) used a spinning flywheel to impact the experimental fault, so that a finite amount of energy was supplied.

High-velocity experiments have revealed fundamental features of dynamic friction:

1. The dynamic friction strongly depends on slip-velocity, and in many cases, the frictional strength approaches very low values as slip-velocity reaches seismic velocities of ~ 1 m/s (Di Toro et al., 2011; Liao et al., 2014; Reches and Lockner, 2010; Sone and Shimamoto, 2009).

2. Dynamic weakening develops over a critical slip weakening distance, D_c, which experimentally ranges from a few cm (Chang et al., 2012) to a few meters (Niemeijer et al., 2011).

3. The frictional strength depends on the rock composition (Di Toro et al., 2004), and slip conditions, e.g., temperature, water presence and normal stress (Reches and Lockner, 2010).

These high-velocity experiments have shown slip histories more representative of natural faults, because variable velocity is closer to natural conditions than constant loading rates. In addition, a variable velocity is needed for the faults to undergo a more realistic evolution of friction, including weakening, strengthening and dynamic healing (Liao et al., 2014; Sone and Shimamoto, 2009). Initial strengthening imposes a barrier for rupture growth into larger earthquakes and weakening is required for acceleration of fault motion, and finally, dynamic healing prevents the fault from continuous slip.

High-speed rotary shear experiments advanced the understanding of earthquake physics; however, there are several open questions to be experimentally addressed. For example, what is the relevant loading procedure for earthquake simulation? What are the constitutive laws for earthquake rupture? My research attempts to contribute to these questions as outlined below.

Present thesis

Objectives

Developing realistic earthquake experimental loading

Stick-slip experiments, in which the stress builds up until fault strength is exceeded (Brace and Byerlee, 1966; Ohnaka et al., 1987), are probably the best simulation style of natural earthquakes. However, classical stick-slip has its own

limitations, including sub-seismic slip-velocity and limited displacement (~ 10 μm). This lack of mechanical intensity can be compensated by high-speed rotary shear experiments, with mechanical power levels that are comparable with natural cases to activate chemical reactions not observed in classical stick-slip experiments. Typical high-speed systems have limitations as well: they typically can control either velocity histories or energy history, but in natural systems, faults do not receive "commands" regarding slip velocities or stress evolutions. In this research, I apply power-density control loading, which is a new technique that allows the experimental fault to respond spontaneously to supplied energy-flux = power. As a result, the power-control loading generates stick-slip events of large displacement (~ 1 m) and seismic velocity (~ 1 m/s) as shown in the results.

Understanding shear rupture propagation

Fault rupture processes are affected by the presence and failure of asperities as demonstrated by (Dieterich and Kilgore, 1994; McLaskey and Glaser, 2011; Rubinstein et al., 2011). My research will expand these capabilities by installing and monitoring high frequency, 3D accelerometers that allow visualizing the shear rupture propagation. I will address questions like: what is the relationship between rupture speeds and slip rates, how is rupture propagation related to loading history, and what information can the acoustic emissions from the high-speed experiments provide in terms of seismic parameters of the experiment.

Organization

Chapter 1 Introduction

This chapter briefly introduces earthquake science with emphasis on rock mechanics experimentation, including basic concepts and history of experimental development.

Chapter 2 Experimental methodology

This chapter outlines the experimental set-up including loading system, control and monitoring system, samples, and the limitations of the machine. The methodology of PD control loading and acoustic emission analysis are the last part.

Chapter 3 Stick-slip events

This chapter presents results of power-density control loading experiments and analyzes two types of stick-slip events. After this part, a spectrum of stick-slip events will be shown at different PD levels, including statistical analysis of a database of stick-slip events in PD control experiments.

Chapter 4 Acoustic emission analysis

Here, I first present rupture size analysis associated with AEs in a typical PD control experiment with AE data. Then, the hypocenter location results and rupture propagation visualization are presented. Another analyzed aspect is the spectral analyses of AEs. Finally, I show initial AE analysis for velocity-control experiments.

Chapter 5 Discussion and conclusion

The discussion focuses on energy budget in PD control experiments and the implication of the experimental results on earthquake sciences. Specifically, I discuss how PD affects fault behavior and how is it related to the earth crust.

Chapter 2 Experimental methodology

Experimental set-up

Overview

Experiments designed to simulate earthquake rupture processes are conducted on the OU high-speed, rotary shear apparatus (ROGA in Fig. 2.1A). It can apply shear along rock blocks at slip-velocities up to 2 m/s, normal stresses up to 30 MPa, and large slip distances. A unique design of the ROGA system is the ability to request the mechanical power dissipated by the fault slip using a real-time, feedback method, called power-density (PD) control loading. This method allows for programmed loading history of energy-rates that create direct response of the experimental fault. Under low PD, the fault may exhibit creep at low velocity and with a high frictional strength, while under high PD, the fault may develop stick-slip events with complex velocity and friction histories. More importantly, the development of either stable sliding or stick-slip is spontaneous under controlled and often constant PDs.

Loading system

The apparatus frame is 1.8 m tall with two decks that are connected to each other by four internally enforced legs. The sample is placed between the two decks, and it is loaded by the rotary power train from below and by the normal stress from above. The power system includes:

(1) A 100 HP three-phase electric motor and controller that provides constant torque of up to 3,000 Nm from 0 RPM to 3300 RPM. The shaft is powered by the motor with 1:6 velocity reduction sprockets.

(2) A 225 kg flywheel to boost the motor torque for short rise time during high-speed tests.

(3) An electro-magnetic large clutch (Ogura) that is capable of full engagement in 30 ms.

(4) A hydraulic piston system (Enerpac) with axial load up to 9,500 N.

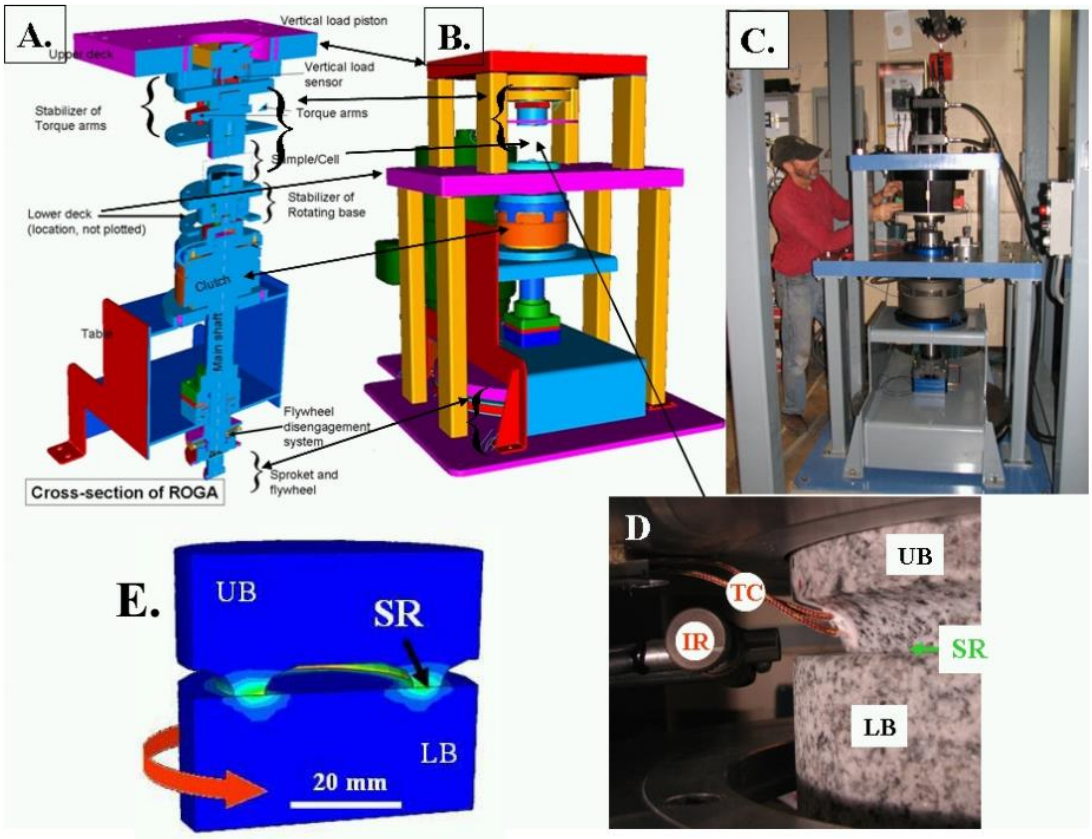

Fig. 2.1 The rotary shear apparatus (Reches and Lockner, 2010). A. Cross section displaying power train. B. 3D view of the assembled apparatus. C. The apparatus with builder Joel Young. D. Sample blocks assembled in the loading frame. LB-lower block; UB-upper block; SR-sliding ring; TC-thermocouple wires; IR-infra red sensor. E. Sample design shown as vertical cut-through of two cylindrical blocks of solid granite rock. The colors indicate temperature distribution due to frictional heating calculated using a finite-element model.

Control and monitoring system

National Instruments control and monitoring system with a SCXI-1100 with modules 1124 (analog control) 1161 (relay control), 1520 (load cell/strain gauge), and

1600 (data acquisition and multiplexer), as well as a USB-6210 (encoder measurements). A dedicated LabView program controls the system. Digital sampling rates of up to 10 kHz are available. Load-cells for axial load and torque (Honeywell), gouge dilation/compaction is measured with four eddy-current sensors (Lion Precision) (1-micron accuracy), temperature measurement is with thermo-couples (Omega), and sample radial velocity encoder (Sick-Stegmann).

In my experiments, there are two cases with eddy current sensors, one of which is using two eddy sensors on top, monitoring fault-normal dilation. The other is using an extra eddy sensor (Eddy 2 in Fig. 2.2b, c) to monitor fault parallel motion, which is equivalent to elastic deformation when there is no frictional motion.

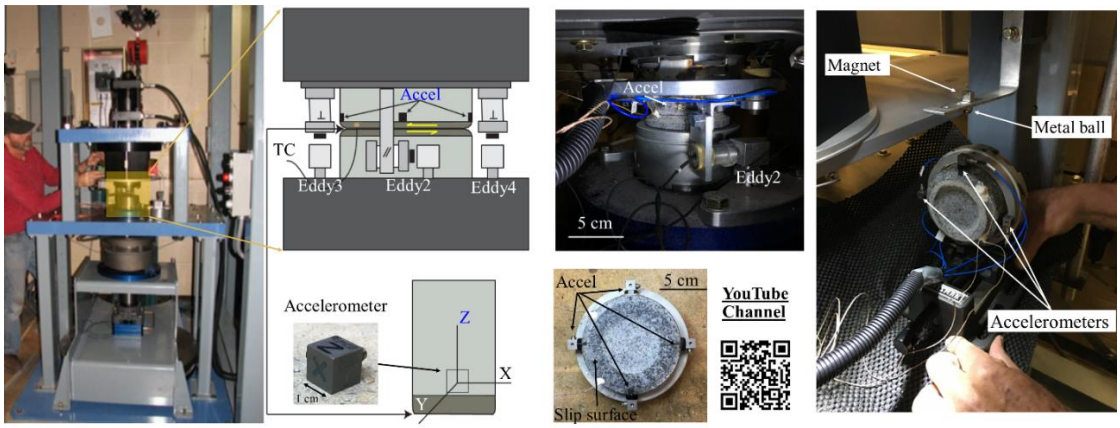

(a) (b) (c) (d)

Fig. 2.2 (a) ROtary Shear Apparatus (ROGA) (Reches and Lockner, 2010), the same as Fig. 2.1C. Shown here as a reference only. (b) Schematic diagram of experimental fault samples with Eddy sensors (Eddy), accelerometers (Accel), and thermal couple (TC). (c) Experimental fault setup (upper photo) and top view of upper block with 4 accelerometers (lower photo). (d) Ball drop test for CBD velocity calibration.

Limitations

The strength of the rock samples limits the performance of the ROGA apparatus. Since the samples are not confined, and there is not always seamless contacting between the upper block and lower block, the records of data shows chattering when the velocity approaches that of seismic slip velocities. Different degrees of chattering, or wobbling, are inevitably present in some of the experiments.

Samples

Samples in the experiments are solid rock blocks as opposed to powder samples. The rock types are as follows.

1. Sierra White Granite (SWG)
2. Charcoal Black Diorite (CBD)
3. Brown Lueders Limestone (BLL)

Each sample includes two cylindrical blocks, diameter=101.6 mm, height=50.8 mm. The upper block has a raised ring with ID=63.2 mm and OD=82.3 mm (Fig. 2.1D, E); the two blocks are pressed across this raised ring. This ring-shape design has an advantage of generating approximately uniform slip-velocity. Because linear velocity is proportional to the radius, due to uniform angular velocity from the motor, a small diameter difference minimizes the linear velocity difference at ring edges of the sample. Thermocouples are cemented into holes drilled 3 mm and 6 mm away from the sliding surfaces (Fig. 2.1D).

Power-control loading

Methodology

A unique tool in the loading procedure brings our experiments closer to natural earthquakes. The experimental fault will be loaded by power-density-control while the

evolution of both slip-velocity and frictional strength will be determined spontaneously by the experimental system without operator intervention. The rate of energy dissipation (=power) per unit area of the fault has units of MW/m^2, and is calculated by

PD = Power-density = [slip-velocity] * [shear stress].

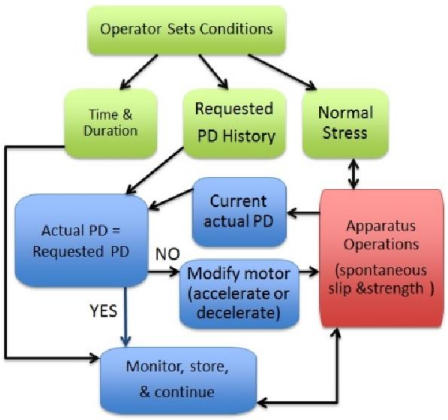

Fig. 2.3 PD control algorithm. Note that the green operations are done before the experiment, the red part is done on the apparatus, and the blue part is the feedback control implemented in the dedicated program on PC.

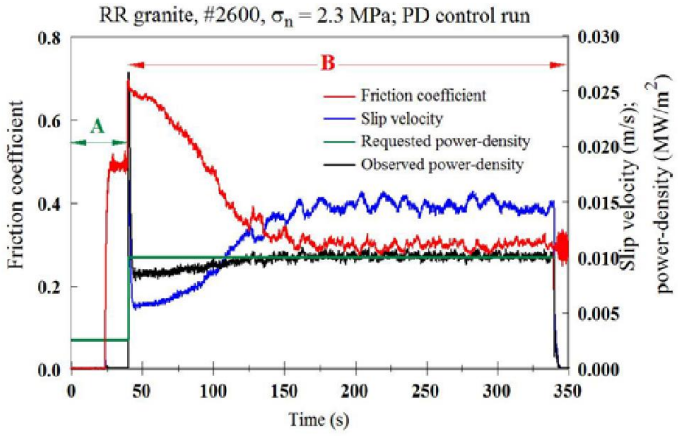

Fig. 2.4 A typical PD control experiment. See text for details.

The apparatus motor has a controller with a feedback control on either torque or velocity. The operation and data acquisition is controlled with a dedicated LabView program in which we programmed a ‘proportional–integral–derivative’ (PID) controller

for the PD controlled experiments (Fig. 2.3). The actual PD is calculated continuously at up to 256 Hz during the experiment, and it is compared to the requested PD history. The most important advantage of this procedure is that the operator only selects the requested PD history and both the frictional resistance (including dynamic changes) and the slip-velocity are controlled by the experimental fault. This PD control procedure is flexible, and with variation of the PID parameters, the system can generate quasi steady-state slip (Fig. 2.4), or unstable slip as shown below in the results (Fig. 2.5a).

Behavior of PD control loading

There are different behaviors of the experimental fault due to specific functioning of PD control loading. One limitation of the present PD control loading system is a delay of calculation of actual PD by the lab computer. There is approximately 0.3-s delay between the outcome of current actual PD and the receipt of signals like torque (equivalent to shear stress) and motor speed. This delay is part of the reason of the development of the spontaneous stick-slips. Another reason is PID parameters (Proportional-Integral-Differential). Since PID controls how the motor responds to the past, present and future values of current PD, the PID values are crucial to the behaviors of PD control loading. It is empirically determined that PID values of 4, 1, and 0 produce best stick-slip behavior in the ROGA system. A third reason is regarding rock mechanics. When the rock sample is strong, or un-weakened, stick-slip tends to develop, while when the sample is already weak due to long distance sliding shortly before, the behavior is prone to stable sliding instead of jerky motion like stick-slip. Fig. 2.5a shows an example of un-weakened stick-slip in a 10-s window where the friction is about 0.7. A displacement of ~1.6 m was accumulated on the fault in a

continuous run after this experiment 3439. Fig. 2.5b shows an experiment after the long sliding with weakened stick-slip of peak friction of 0.33. After the distance of 2.5 m accumulated due to experiment 3446, the fault showed stable sliding under constant PD with a friction of 0.35 (Fig. 2.5c). The implication of this transition is to be discussed in the discussion section.

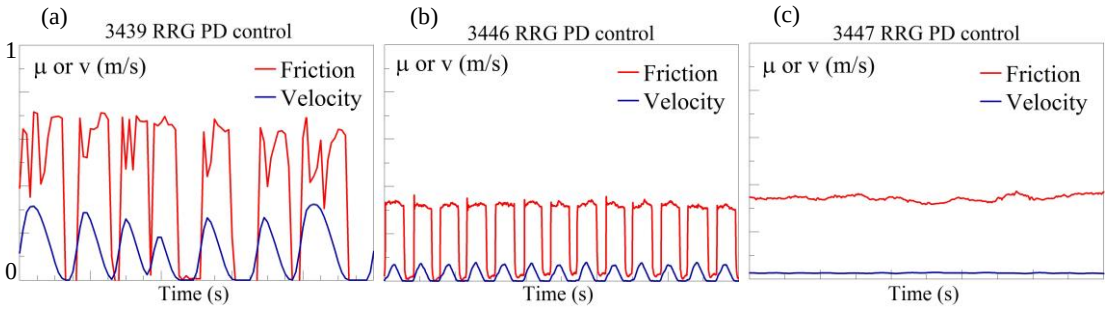

Fig. 2.5 Behavior of PD control. (a) Un-weakened stick-sip (b) weakened stick-slip (c) stable sliding.

Acoustic emissions

Acoustic emissions measurements

A recent upgrade to ROGA's capabilities includes addition of four 3D miniature accelerometers glued at distance of 2.0 cm from the experimental fault (Fig. 2.2b, c). The accelerometers are model 356B21 of PCB Piezotronics with sensitivity of 10 mV/g and range of ± 500 g. The accelerations in X, Y, and Z directions are recorded at rates up to 8 MHz with a dedicated PC. These measurements are plotted into accelerograms (e.g. Fig. 2.6) where one can observe multiple acoustic emissions (AEs). With the AE phenomena, ball drop tests (McLaskey et al., 2015) were used to calibrate the seismic wave velocities within the sample rocks (Fig. 2.2d). These accelerometers already provide critical data on rupture characteristics.

Hypocenter locating algorithms

The acoustic emissions recorded during the experiments provide a method to locate the hypocenters of each AE. The importance of locating those AEs is related to

fault rupture propagation. Fault rupture processes are affected by the presence and failure of asperities as demonstrated by (Dieterich and Kilgore, 1994; McLaskey and Glaser, 2011; Rubinstein et al., 2011). Slip of the experimental fault begins with the breakdown of an asperity, and this initial breakdown is of great importance because it provides unique information about the whole fault slip. The initial AE can be detected with the accelerometers near the experimental fault surface. Thus, temporal and spatial distribution of the AEs is crucial for understanding rupture of asperities.

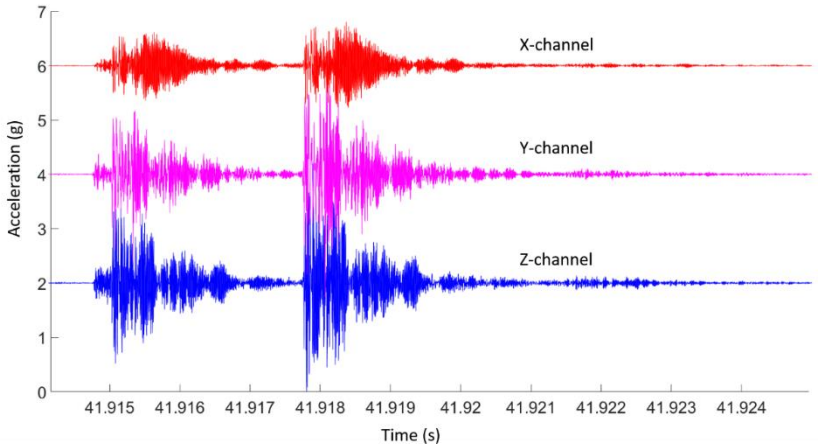

Fig. 2.6 An example of accelerograms. The figure shows three channels (directions) of one accelerometer during 0.01 s of an experiment. Absolute values on the vertical axis are arbitrary.

In my experiments, four miniature 3D accelerometers are mounted on the sidewall of the stationary rock sample block. They serve as "seismic stations" located just centimeters away from the experimental fault. We assume that the AEs occur on the interface of the two rock sample blocks, thus downgrading the problem to a 2D problem (Fig. 2.7). Numbered boxes 1 ~ 4 are accelerometers and a Cartesian system is established. I assume the AE occurs at point P. With simple examination of the geometry, the following equations can be obtained.

$$\frac{\sqrt{(x_0 - x_i)^2 + (y_0 - y_i)^2 + \Delta z^2}}{v_p} = t_i - t_0, i = 1,2,3,4$$

Known variables are location coordinates of the accelerometers, x_i, and y_i, vertical offset, Δz, p-wave velocity of the sample rock from calibration, v_p, and absolute first arrival times from hand picking, t_i. Only three variables, location of AE, x_0, y_0, and time of occurrence, t_0, are unknown, whereas there are four equations (i = 1,2,3,4). Therefore, the system of equations is overdetermined. In order to solve the problem, first, I make an initial guess of x_0 and y_0, calculate t_0 for each of the four accelerometers, and then calculate the standard deviation of t_0, $\sigma(t_0)$. In theory, $\sigma(t_0)$ should be zero because the time of occurrence is the same for different "seismic" pathways. So I use a method of unconstrained nonlinear optimization (a grid search, or simplex search method) to minimize $\sigma(t_0)$ while changing the values of x_0 and y_0 from the initial guess. The values of x_0 and y_0 when a minimal $\sigma(t_0)$ is achieved are the calculated hypocenter of the corresponding AE. (More information is available in the appendices including description and instruction of two MATLAB programs for analyzing AEs and obtaining AE hypocenters.)

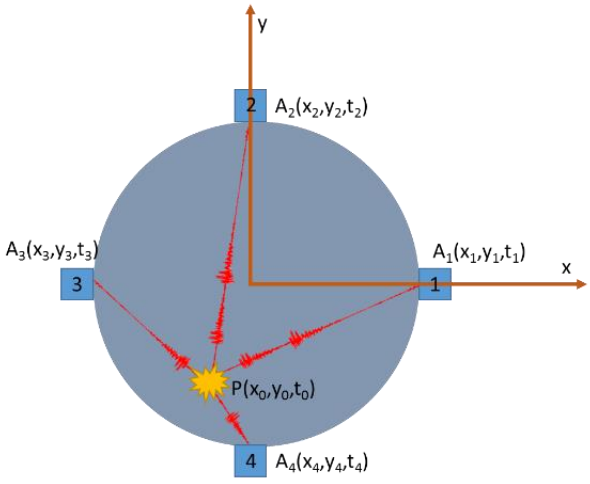

Fig. 2.7 Hypocenter locating diagram. Yellow star is the source of AE. Red trains are waves propagating from the source to the four accelerometers (stations).

Chapter 3 Analysis of experimental stick-slips

Stick-slip events in power-density control experiments

A typical PD control experiment

Fig. 3.1 displays a typical power-density control loading experiment in experiment #3505 on a diorite experimental fault. Two levels of power-density were applied here: a low level initial stage of 0.006 MW/m^2, for 20 s, followed by a high level stage of 0.15 MW/m^2 for 20 seconds (green curve in Fig. 3.1). A total of 28 spontaneous slip events occur upon the request of power-density and the friction coefficient (red) and velocity (blue) evolutions are plotted in Fig. 3.1.

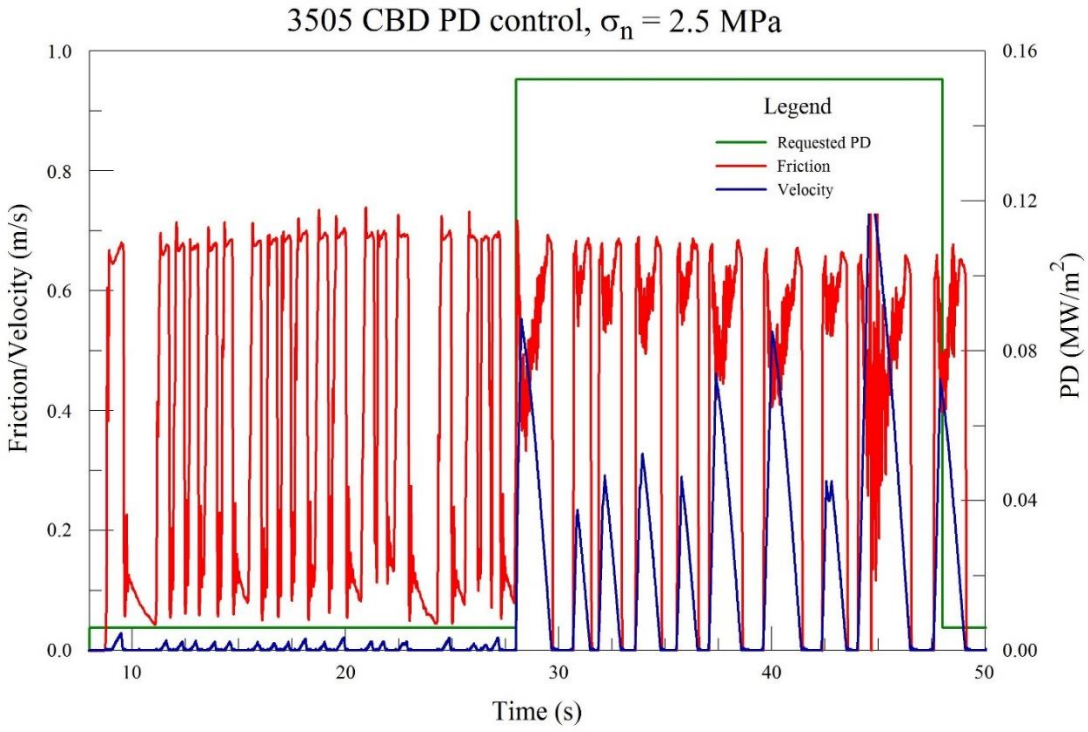

Fig. 3.1 A typical PD control experiment. See text for details.

Two types of slip-events (Figs. 3.2, 3.3) that correspond to the two levels of requested PD were recognized in this experiment. The low PD slip-event begins with the accumulation of shear stress (friction), in a gradual rise and impulsive fall of friction

(red in Fig. 3.2). Pre-slip events (orange arrows) preceding the peak friction. At peak friction, the main slip initiates. As slip ceases, friction evolves as the machine relaxes. Due to the low slip-velocity (< 1 cm/s) and short displacements (< 1mm) of these slip-events of the low PD, we term them as 'creep events' with three stages: foreshocks, main slip, and aftershocks.

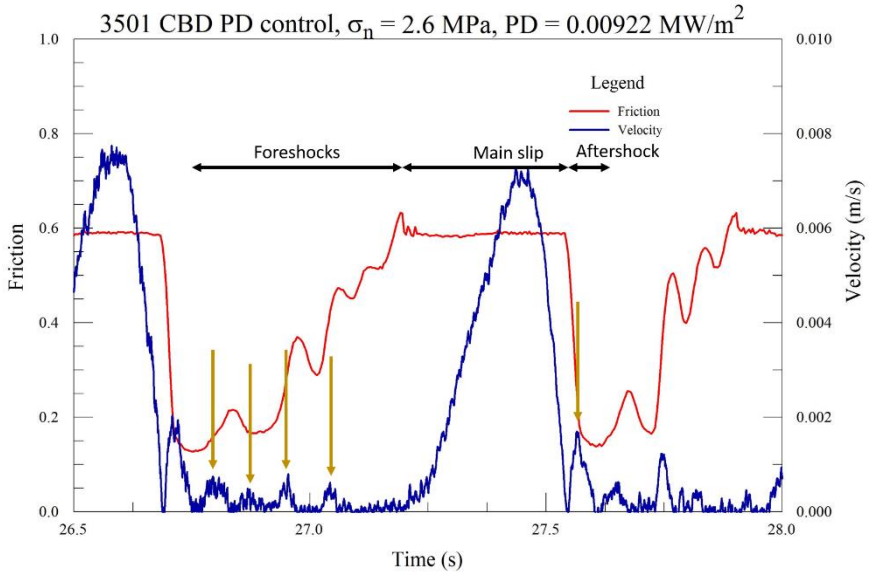

Fig. 3.2 Creep events in low power-density. Note different scales of friction and slip-velocity.

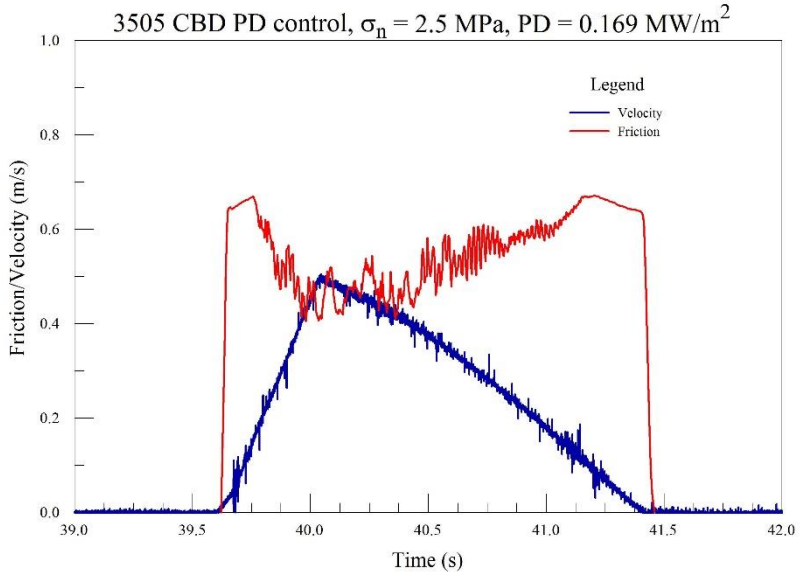

Fig. 3.3 Micro-seismic stick-slip events in high power-density.

Under high requested power-density, the slip-events (Fig. 3.3) display intense acceleration and associated weakening that are followed by deceleration and strength recovery. Both the slip-velocity (up to 0.6 m/s) and displacement (~ 0.4 m) are equivalent to those of moderate earthquakes (M=3-4), and thus termed 'micro-seismic stick-slip' or 'stick-slip'. This behavior of weakening followed by strengthening is typical to 'slip-pulse' mode (Liao et al., 2014). The difference and similarities of the two events types are summarized in Table. 1.

Table 1 Comparison of creep events and micro-seismic stick-slip events

Characteristics	**Creep events**	**Stick-slip events**
Requested power	Low	High
Fore-shocks/After-shocks	Yes	No
Slip-velocity	Low (~ 1 cm/s)	High (0.5~0.8 m/s)
Displacement	A few mm	~0.5 m comparable to seismic
Weakening	A few %	>30%
Acceleration	Slow	Fast

Spectrum of behavior of stick-slip experiments

In the present study, a PD range of 0.0002 – 0.17 MW/m^2 was applied on two rock types: granite (RRG) and diorite (CBD). Figure 3.4 displays the experimental results in which from top to bottom the PD increases from low to high levels, and the left and right columns are for CBD and RRG, respectively. The horizontal scale (time at 5 s) and vertical scale (friction coefficient and slip-velocity) are fixed scales for all subsets for easy comparison.

Generally, the change in patterns from low to high PD levels reflects a transition from creep events to micro-seismic stick-slip mentioned above. The higher the PD level, the more weakening occurs in the fault strength and the higher the slip-velocity. One exception is when PD increases from experiment 3490 to 3500, both velocity and weakening decrease. Moreover, CBD and RRG experiments show similar trends in terms of velocity and weakening with increasing PD. The frequency of stick-slip occurrence is 1 – 5/5s, or equivalently 0.2 – 1 Hz and it shows no trend with increasing PD.

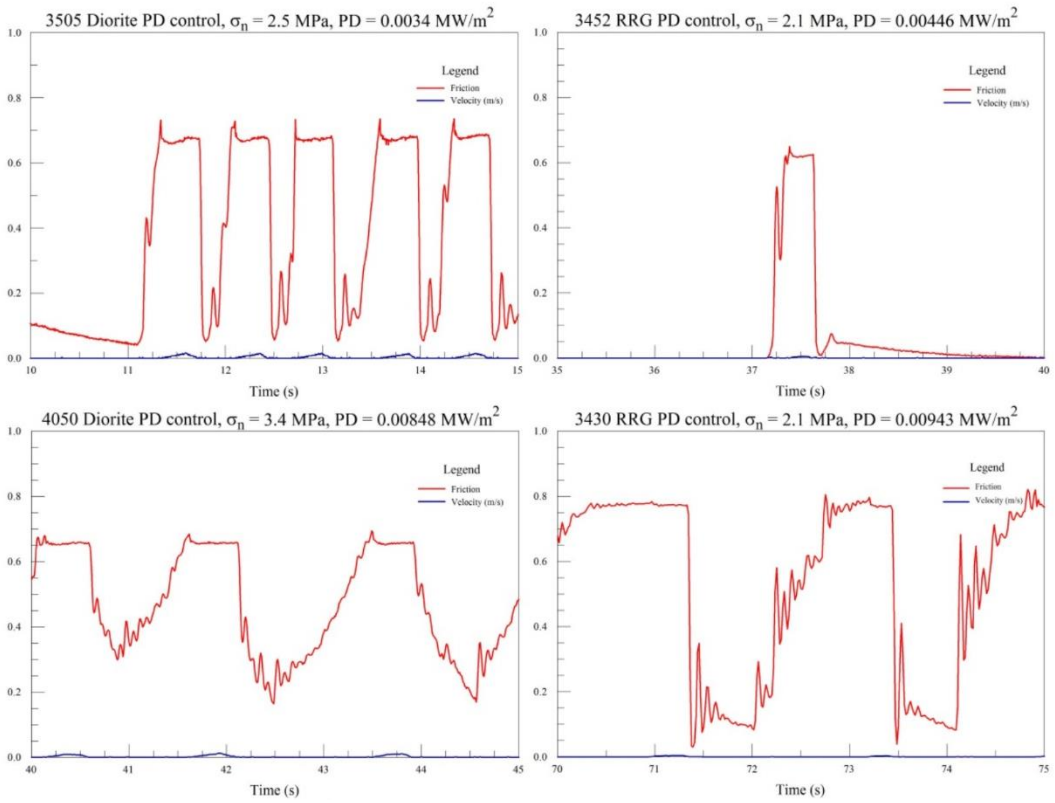

Fig. 3.4a A spectrum of PD control experiments. See text for details.

Statistics of the stick-slip events

We conducted 39 runs with Radiant Red Granite and 37 runs with Charcoal Black Diorite. Slip-events have slip displacements ranging 0.0001– 1.3 m. A requested

range of PD's, 0.0045 – 0.17 MW/m^2, were applied in exponential spacing to perform statistical analysis of the stick-slip events. I picked the same number of slip-events from each PD level in the range for both RRG and CBD (8 events per PD level for RRG and 10 for CBD). I then collected mechanical data of each slip-event, e.g. shear stress, friction drop, temperature, peak velocity, forming a database of 42 CBD stick-slips and 19 RRG stick-slips ready for analysis.

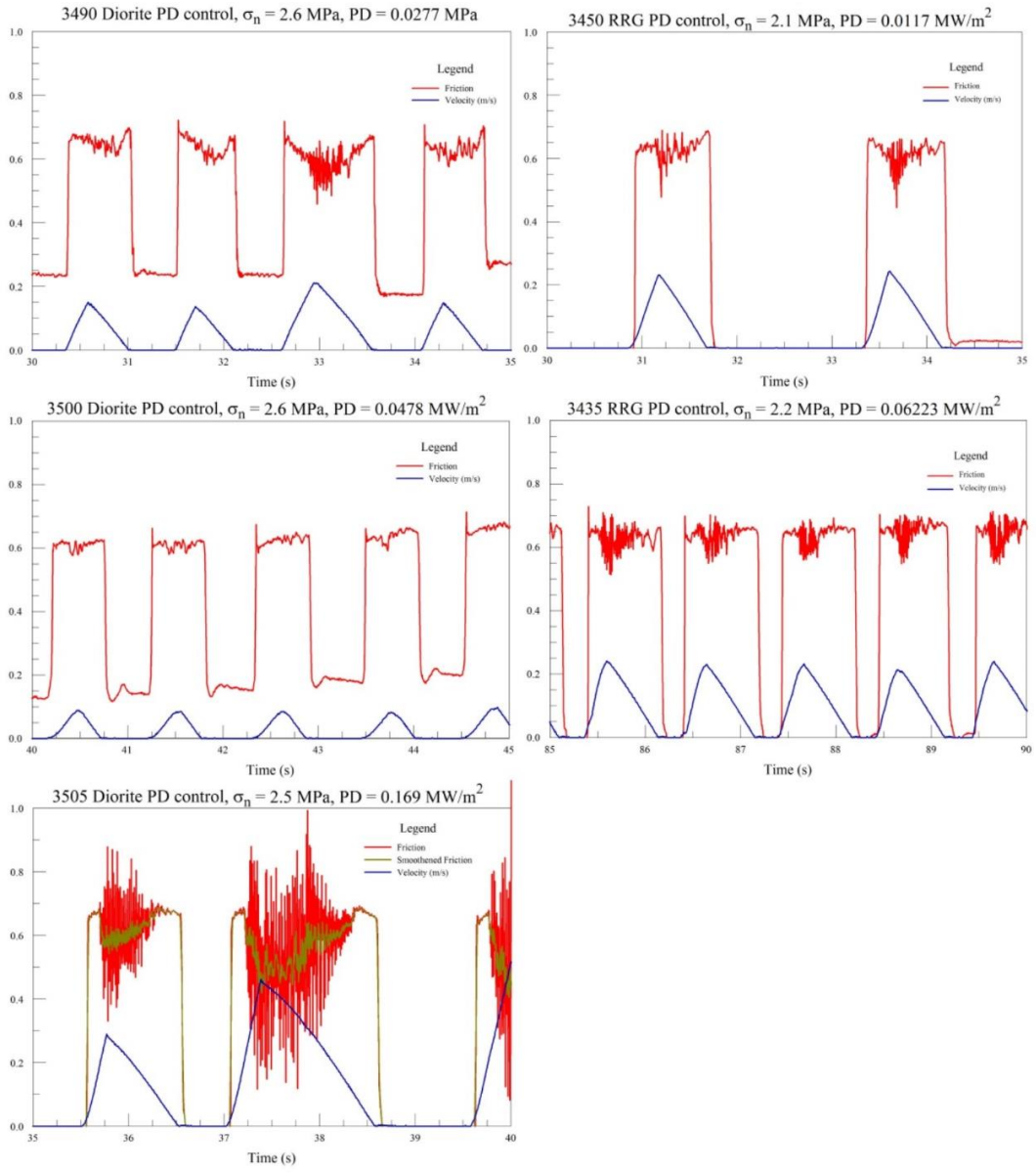

Fig. 3.4b A spectrum of PD control experiments (continued). See text for details.

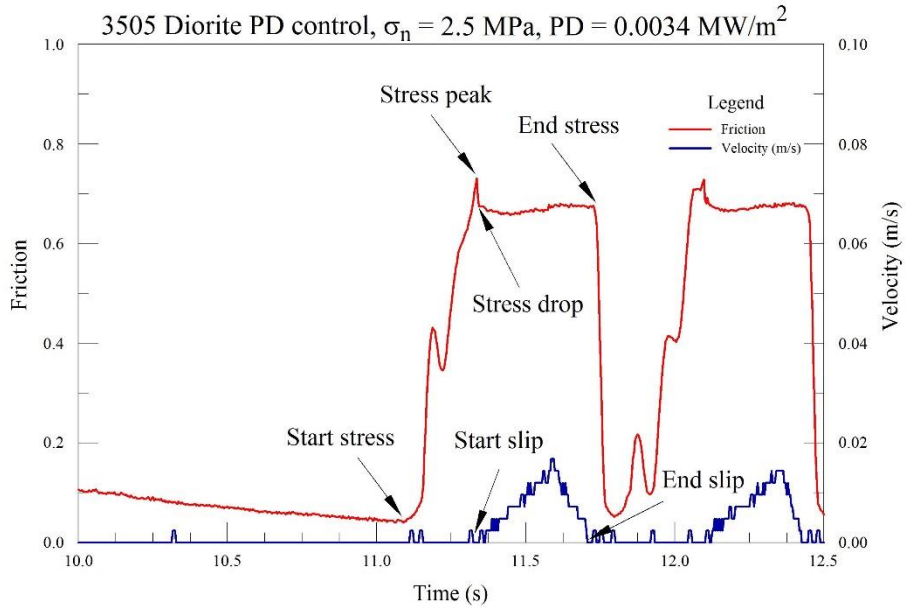

Fig. 3.5 Event picking protocol for creep events.

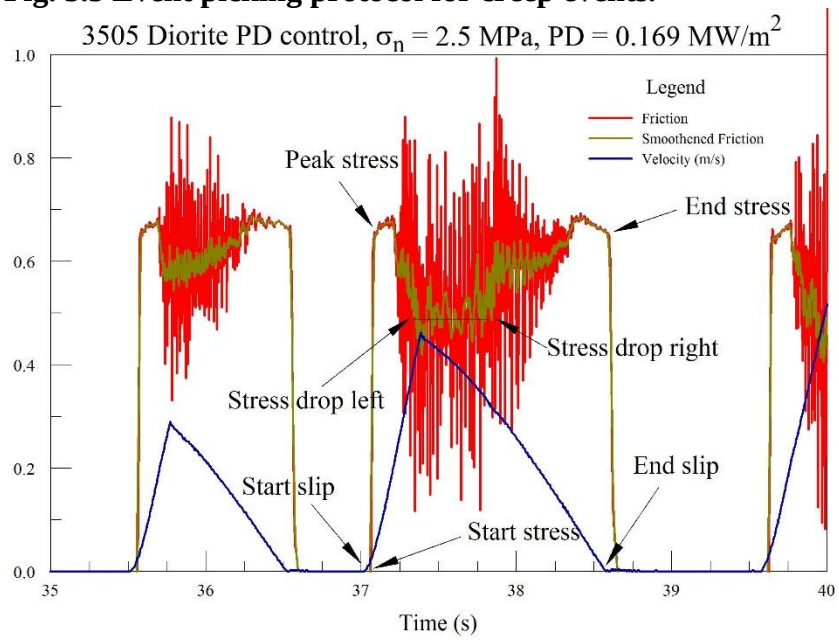

Fig. 3.6 Event picking protocol for micro-seismic stick-slip.

The critical points on each stick-slip event are shown in Fig. 3.5, 3.6. Creep events (Fig. 3.5) have six picked points. Note that end stress point and end slip point are very close to each other in time, so I use end slip for both positions. This reduces the number of points to five points. Micro-seismic stick-slip events (Fig. 3.6), have seven

picked points, and here, start slip, start stress, and peak stress are quite close to each other in time, and end stress and end slip are also close, so I only use start slip and end slip in the analysis. This makes four points instead of seven. The following parameters are defined for the analysis:

Friction drop = friction(stress peak) – friction(stress drop);

Mean friction = mean(friction(start slip:end slip));

Rise time = time(end slip) – time(start slip);

Distance = distance(end slip) – distance(start slip);

Peak velocity = max(velocity(start slip:end slip));

Friction vs slip distance

The mean friction displays gradual decrease with increasing slip distance for CBD (Fig. 3.7), which may suggest that larger events of long slip distances underwent more weakening. For slip distances of 0.0001 – 0.1 m, the rate of friction decrease is relatively slow, and the rate increases for distances of 0.1 – 1 m. At a maximum slip distance in my picked events, a slip distance of about 1 m corresponds to the lowest mean friction of 0.5. The decreasing trend is distinct for CBD events while there is more scattering for RRG events. From 0.0001 – 0.001 m, there are two levels of points away from the CBD trend, but at around 0.1 m the friction of RRG is at the same level of CBD.

Friction drop vs slip distance

Fig. 3.7b shows a plot of friction drop against slip distance for stick-slip events from PD control experiments on the CBD and RRG samples. The friction drop remains roughly constant, ~ 0.05, for slip distances < 0.01 m, and it increases with the slip distance for slip distances 0.01 – 1 m; maximum friction drop is 0.35 at a distance of 1.1

m. We noted that the transition to increasing friction drop corresponds to the event type transition from creep events to micro-seismic stick-slip.

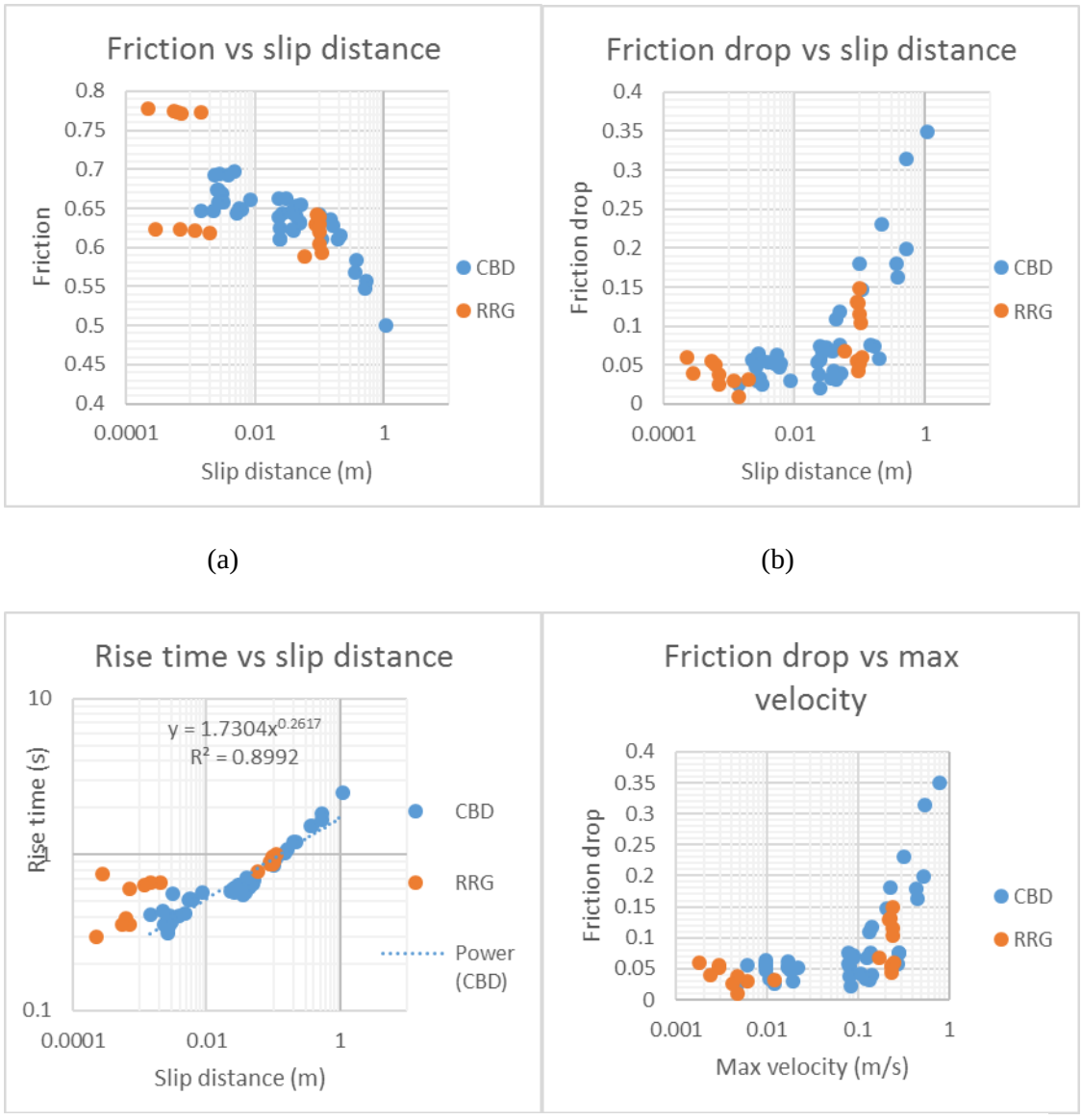

(a) (b)

(c) (d)

Fig. 3.7 (a) Friction vs slip distance (b) Friction drop vs slip distance (c) Rise time vs slip distance (d) Friction drop vs max velocity.

Rise time vs slip distance

Fig. 3.7c shows a plot of rise time against slip distance for the analyzed stick-slip events. Again, the slip distance of ~ 0.01 m indicates a transition from creep events

to micro-seismic stick-slip. Below 0.01 m the points are scattered indicating while above 0.01 m there is a power-law trend between rise time and slip distance.

Friction drop vs maximum velocity

Fig. 3.7d shows a plot of friction drop against maximum (max) velocity for the analyzed stick-slip events. From max velocity of 0.001 – 0.1 m/s, the friction drop of slip events remains at a level of 0.05, while from max velocity of 0.1 – 1 m/s, the friction drop increases with the max velocity. The maximum friction drop is 0.35 at a max velocity value of 0.8 m/s. At the point when friction drop starts to increase with max velocity, the event type transitions from creep events to micro-seismic stick-slip. The behavior is similar to Fig. 3.7b because max velocity is positively related to slip distance.

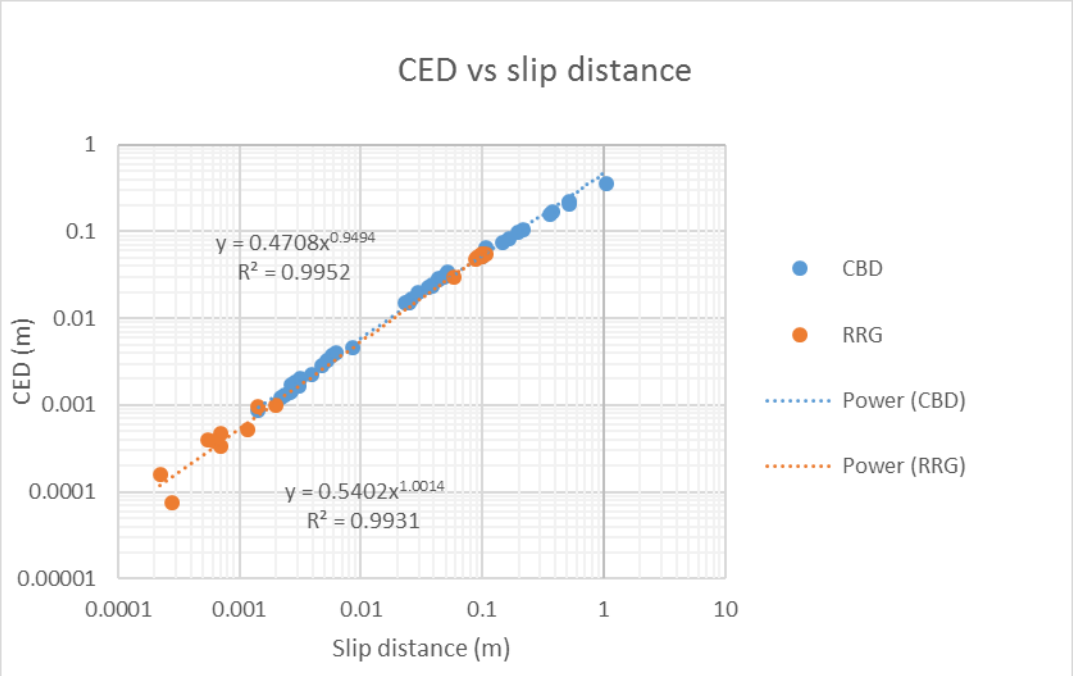

Fig. 3.8 CED vs slip distance.

Coulomb Energy Density vs slip distance

The energy level of the stick-slip events is characterized by the Coulomb Energy Density (CED), which is defined as follows (Chang et al., 2012).

$$CED = \frac{\int_{t_0}^{t_1} \tau \cdot v dt}{\overline{\sigma_n}}$$

In the equation, t_0 and t_1 are start time and end time of a slip event. Symbol $\overline{\sigma_n}$ is the averaged normal stress during the event. τ is shear stress, and v is slip-velocity, both of which are a function of time t. CED has units of m, yet the physical meaning of CED is energy per unit area per unit normal stress. The plot of CED as function of slip distance (Fig. 3.8) displays a clear power-law trend from 0.0001 – 1 m for stick-slip events from both CBD and RRG with fit powers very close to unity. This can be explained by the definition of CED. Assuming constant shear stress, the equation is simplified as follows.

$$CED = \frac{\tau \cdot D}{\overline{\sigma_n}}$$

The above equation shows a linear relationship between CED and D, and the coefficient is shear stress divided by mean normal stress, which is equivalent to the coefficient of friction. The fit powers of unity are the result of this relationship and the coefficients 0.47 for CBD and 0.54 for RRG are equivalent to the averaged friction.

Friction drop vs Coulomb Energy Density

The CED incorporates both kinetic and kinematic properties of the slip event. However, friction drop is measured independently of CED. Fig. 3.9 shows a plot of friction drop against CED for stick-slip events from PD control experiments on the

CBD and RRG samples on a log-linear scale. From CED of 0.0001 – 0.01 m, the friction drop of slip events remains at a level of 0.05, while from CED of 0.01 – 1 m, the friction drop increases with the CED. The maximum friction drop is 0.35 at a CED value of 0.36 m. At the point when friction drop starts to increase with CED, the event type transitions from creep events to micro-seismic stick-slip. This figure looks similar to Fig. 3.8b, d, because CED is proportional to slip distance and max velocity.

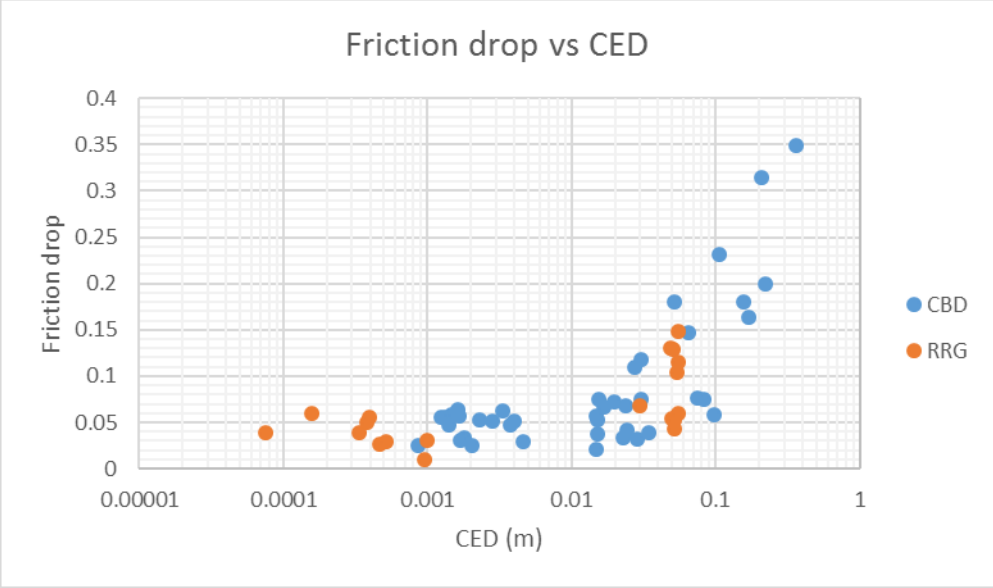

Fig. 3.9 Friction drop vs CED.

Coulomb Energy Density vs Power-density

The response of the experimental fault to the level of requested PD is of great interest because the requested PD is the experimental analog of the rate of tectonic loading for natural earthquakes. The response of the experimental fault, which is represented by CED, is plotted as function of the requested PD in Fig. 3.10. The data is scattered with a general trend of CED increase with requested PD increase. The power fit of CBD events is close to unity. Note that CED is calculated for individual stick-slip events, while the requested PD is for a loading condition under which multiple stick-slip

events develop. The scattering on the figure shows under different requests of power, or energy-rate, the experimental fault tends to incur slip events of different energy levels. This could be due to controlling issues and conditions of rock samples including gouge formation, weakening, heating, etc.

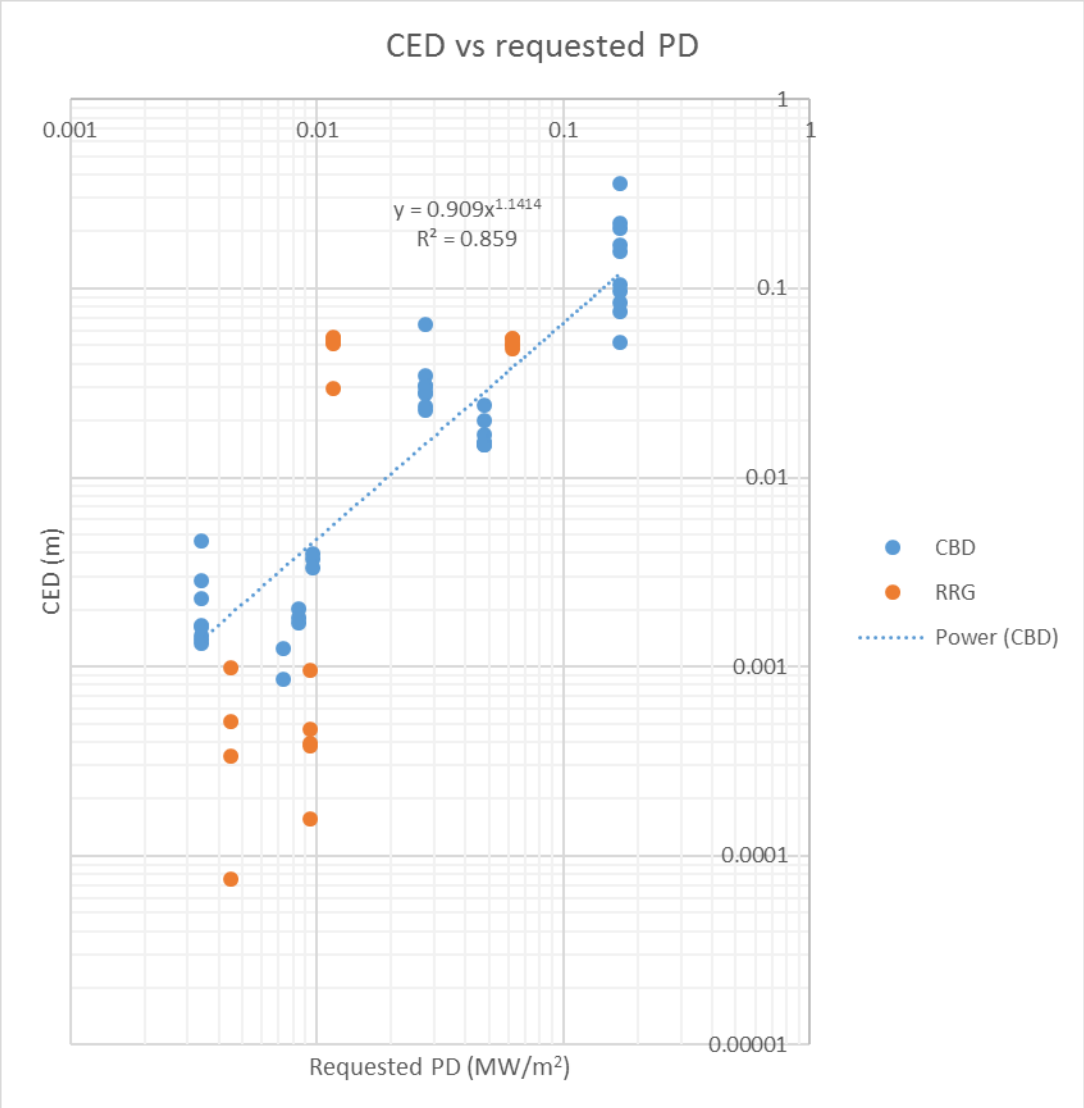

Fig. 3.10 CED vs requested PD.

Chapter 4 Acoustic emission analysis

Acoustic emission in PD control experiments

Hundreds of acoustic emissions (AEs) were recorded during the large stick-slip events by the Installed accelerometers. Fig. 4.1 is a series of progressive zooming images of the AEs together with simultaneous mechanical parameters. In Fig. 4.1b, c, the three horizontal lines with spikes are accelerograms in three directions for one of the 4 accelerometers, red curve is the friction coefficient, blue curve is slip-velocity, and green curve is fault parallel twist (recorded by Eddy2 in Fig. 2.2b, c), which indicates the elastic deformation in microns prior to frictional fault slip. This fault parallel twist accumulates along with friction build-up and it recovers when peak friction value is achieved. Some AEs exceed 500g acceleration; some are tens of g, while others are within the background noise. The biggest AE occurs at the same time as fault parallel twist obtains its peak value. This coupling indicates the onset of main frictional slip stage of the stick-slip.

Rupture size associated with AEs

The stick-slip event of Fig. 4.1b has 97 clear AEs (e.g. the first three in Fig. 4.1d), and 79 suspected AEs (e.g. the last two in Fig. 4.1d). The total slip-distance during the slip event in Fig. 4.1b is 17 mm, thus each AE, on average, represents micro-rupture of ~175 μm (clear AEs only) or ~ 96 μm (all AEs). The relation of rupture sizes of AEs and other mechanical parameters remains to be analyzed.

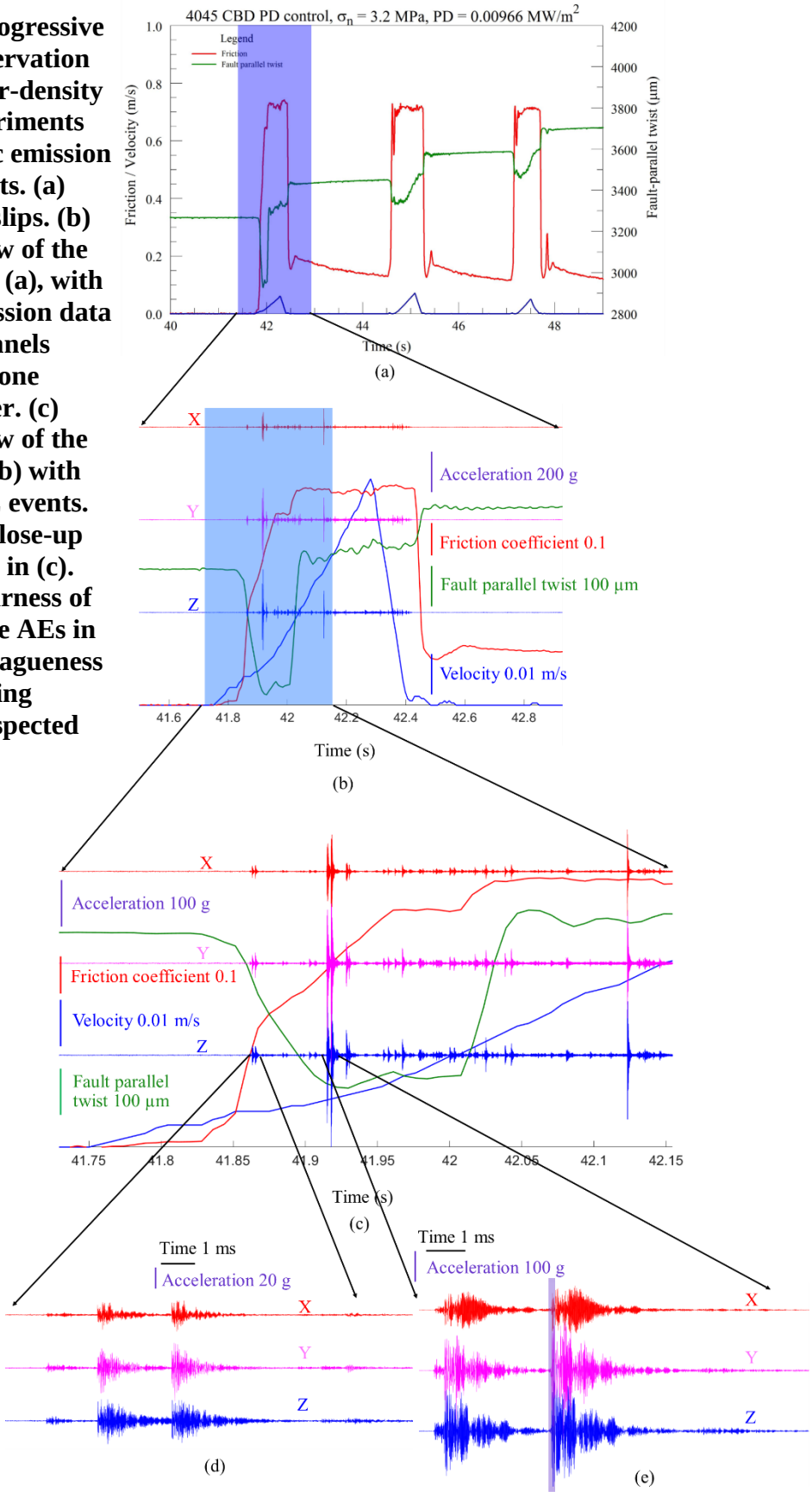

Fig. 4.1 A progressive series of observation during power-density control experiments with acoustic emission measurements. (a) Three stick-slips. (b) Close-up view of the first event in (a), with acoustic emission data of three channels (XYZ) from one accelerometer. (c) Close-up view of the first half of (b) with details of AE events. (d) and (e) Close-up views of AEs in (c). Note the clearness of the first three AEs in (d) and the vagueness of the following siganls of suspected AEs.

AE hypocenter locations

Based on the assumption that the AE sources are ON the experimental fault interface, I located the sources of 14 AEs using time differences of first arrivals of the acoustic signals from the four accelerometers, similarly to earthquake location. Fig. 4.2b displays the location of the 14 early AEs in the stick-slip event of Fig. 4.1b. The 14 AE locations are scattered but generally fall in or close to the fault slipping contact (double, dashed circles). The AE concentrations indicate that the ruptures initiated at two small areas that we interpret as sites of prominent asperities, which radiated the acoustic wave during their failure.

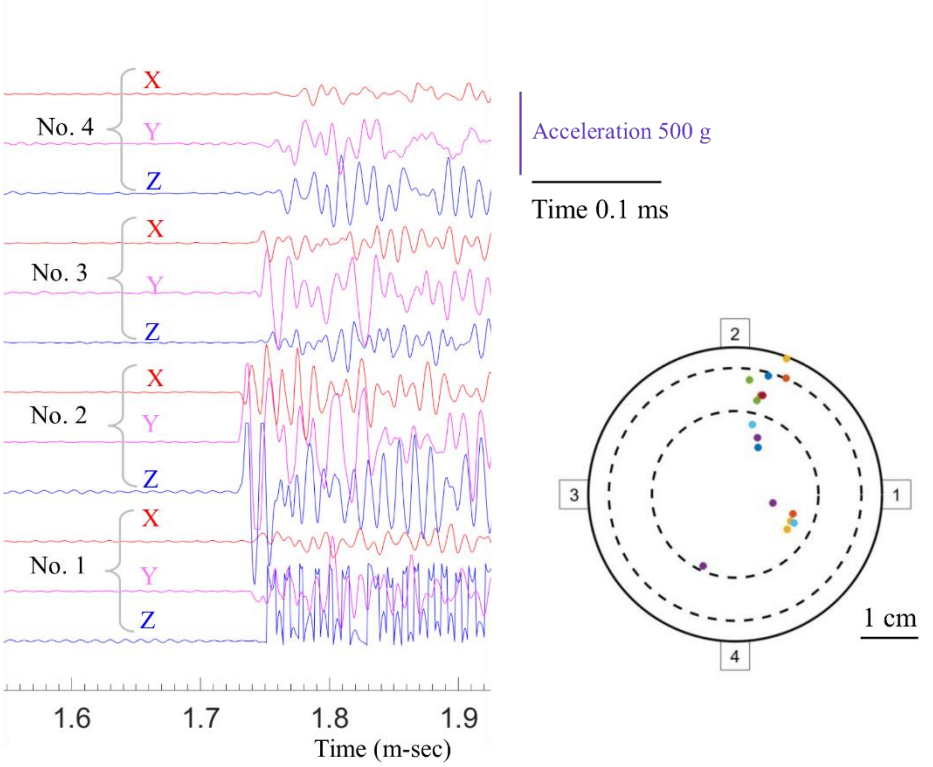

(a) (b)

Fig. 4.2 (a) Time close-up view of Fig. 4.1e showing difference in first arrivals in the four accelerometers. (b) Experimental fault surface with AE locations; boxed numbers 1~4 are accelerometers.

Spectral analysis

The AEs observed in rock friction experiments can be spectrally analyzed by seismological methods, and this analysis could yield seismic moments and source radii of the AEs. This section focuses on my preliminary spectral analysis on AEs, and outlines the spectrograms features and the potential for utilizing AE spectra as tools for obtaining AE source parameters.

I analyzed two sources of AE data, and the first is from ball drop tests (Chapter 2, Fig. 2.2d). Fig. 4.3a shows a time series (upper panel) and corresponding spectrogram (lower panel) of a single AE event from a ball drop test on CBD rock surface. The time series shows a sharp first arrival followed by an exponential decay. The spectrogram displays two curves, the red of which is multi-taper power spectral density spectrum (PMTM) and the black is regular Fourier transform spectrum (FFT) (Percival and Walden, 1993). One can note, a broad, yet spiky peak, around 11 kHz, and a peak around 86 kHz. The latter is the sensor resonant response (Product Specification Sheet of 356B21 PCB Piezotronics), which is not related to actual vibration in the sample, and it is present in all AEs events. Fig. 4.3b is also from a ball drop test on CBD, but here the metal ball was dropped directly on the accelerometer instead of the rock sample. The result is slightly different. The time series shows a distinct first arrival but the spectrogram shows a broad peak at around 10 kHz, and the 86 kHz sensor response are also present.

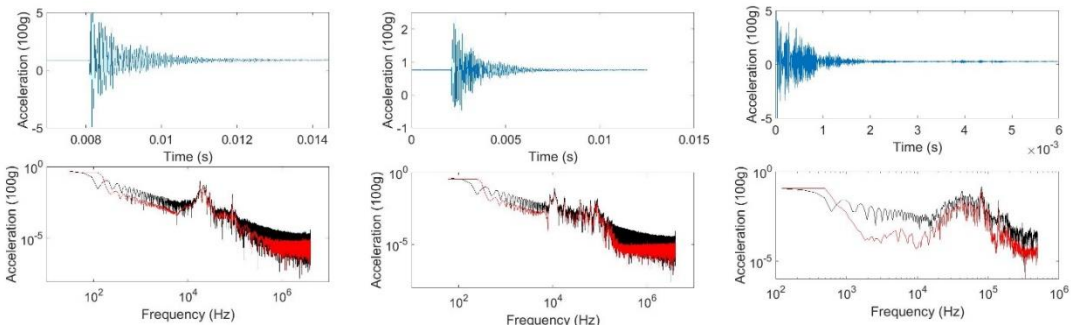

Fig. 4.3 Time series and spectra of AEs in (a) CBD velocity calibration ball drop test on rock surface in transverse direction of the accelerometer (y-direction), (b) CBD velocity calibration ball drop test on accelerometer surface in vertical direction of the accelerometer (z-direction), (c) the event in Fig. 4.2a in transverse direction of the accelerometer (y-direction); red curve is from pmtm method and black curve is from fft method in MATLAB.

Fig. 4.3c shows an AE from a rock friction experiment of run #4045 (Fig. 4.1, 4.2). This plot is of the y-accelerometer, which is in the transverse direction, normal to the slip direction. As expected, the AE in Fig. 4.3c displays more complex pattern than the events of ball dropping. The time series shows a relatively sharp first arrival and the spectrogram has a broad peak from 11 kHz to 100 kHz including the 86 kHz sensor response.

With complex spectral response of AEs in the experiments, it is difficult to separate one event from another without additional information. One way to obtain the individual event response is calculating spectral ratio of two AEs of different magnitudes observed in the same experiment. The assumption behind this method is that the source radius for the smaller event is negligible compared to the larger event (Kane et al., 2013). By taking the ratio of the spectra of the two AEs, it is expected that irrelevant response (e.g. instrument response) will be removed, and only spectra pertaining to the events are preserved. In this way, the smaller AE serves as an

empirical Green's function (EGF) because it contains 'station response' and minimal event information. Fig. 4.4 shows two AEs in a Diorite PD control experiment #4043. The smaller one (Fig. 4.4a) was designated as the EGF, and spectral ratio was derived for a larger one (Fig. 4.4b) and result is shown in Fig. 4.5. The corner frequency is around 180 kHz, and this frequency can be used to calculate seismic moment and source radius of the larger AE (No. 2 in Fig. 4.4b).

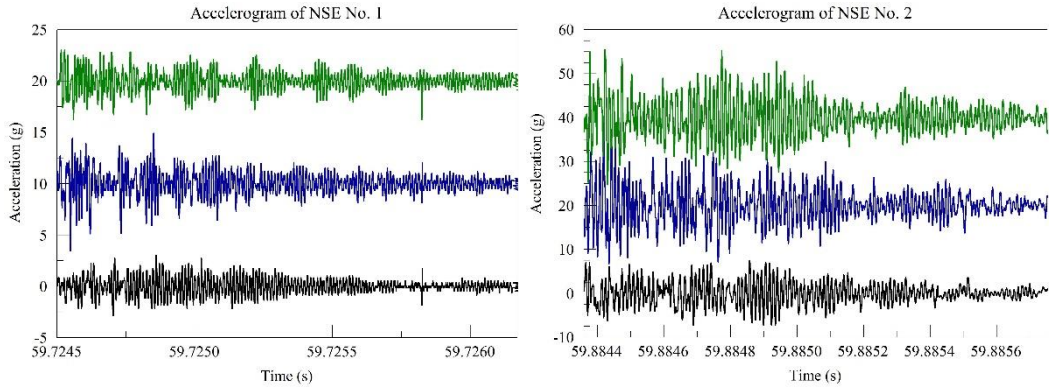

(a) (b)

Fig. 4.4 A small AE (a) and a large (a) with 3 directions shown in 3 curves. Note scale difference. Experiment # 4043.

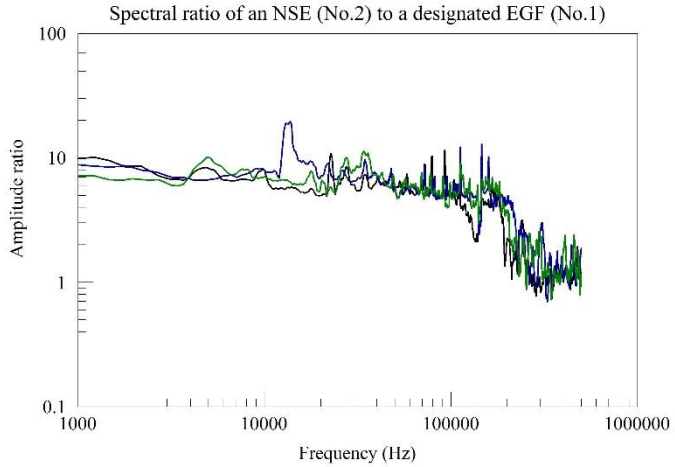

Fig. 4.5 Spectral ratio of two AEs of Fig. 4.4 (as EGF). Experiment # 4043.

Initial AE in velocity control experiments

In velocity control experiments, the slip initiations were frequently accompanied by strong AEs with accelerations that could exceed 500 g (Fig. 4.6). The presence and intensity of these early AEs are apparently related to the mechanical parameters of friction and velocity. Fig. 4.7 shows a series of velocity control experiments on limestone (BLL) in which the slip-velocity increased systematically from 0.001 m/s to 0.61 m/s. One can note that no AEs were recorded in the low velocity runs of #4048 (V = 0.001 m/s) and #4049 (V=0.003 m/s). Run #4050 (V= 0.009 m/s) displayed a single, late, small AE, with no early AE. All runs with V > 0.009 m/s showed early AEs, yet with variable characters (Fig. 4.7). Specifically, the duration and magnitude of the initial AEs did not display systematic relations to the actual slip-velocity. This inconsistency may reflect the situation that these runs were conducted as a series without removing the fault gouge between runs, and the continuous weakening of the experimental fault with slip distance. It is also interesting that the initial AE phenomenon is absent in PD control experiments, even though in theory, it should be present in both types of loading. More work is needed to better understand the behavior of these AEs.

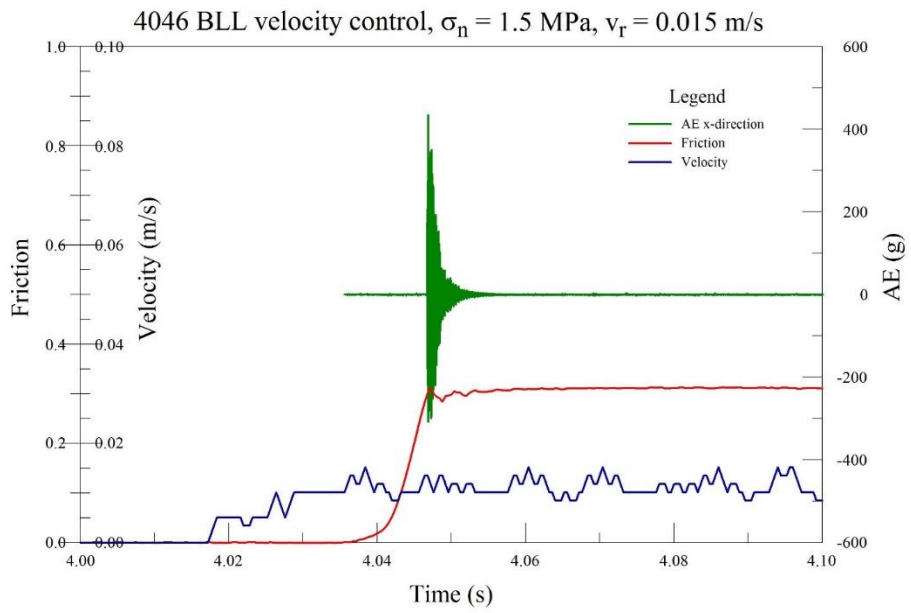

Fig. 4.6 Initial AE in a BLL velocity control experiment.

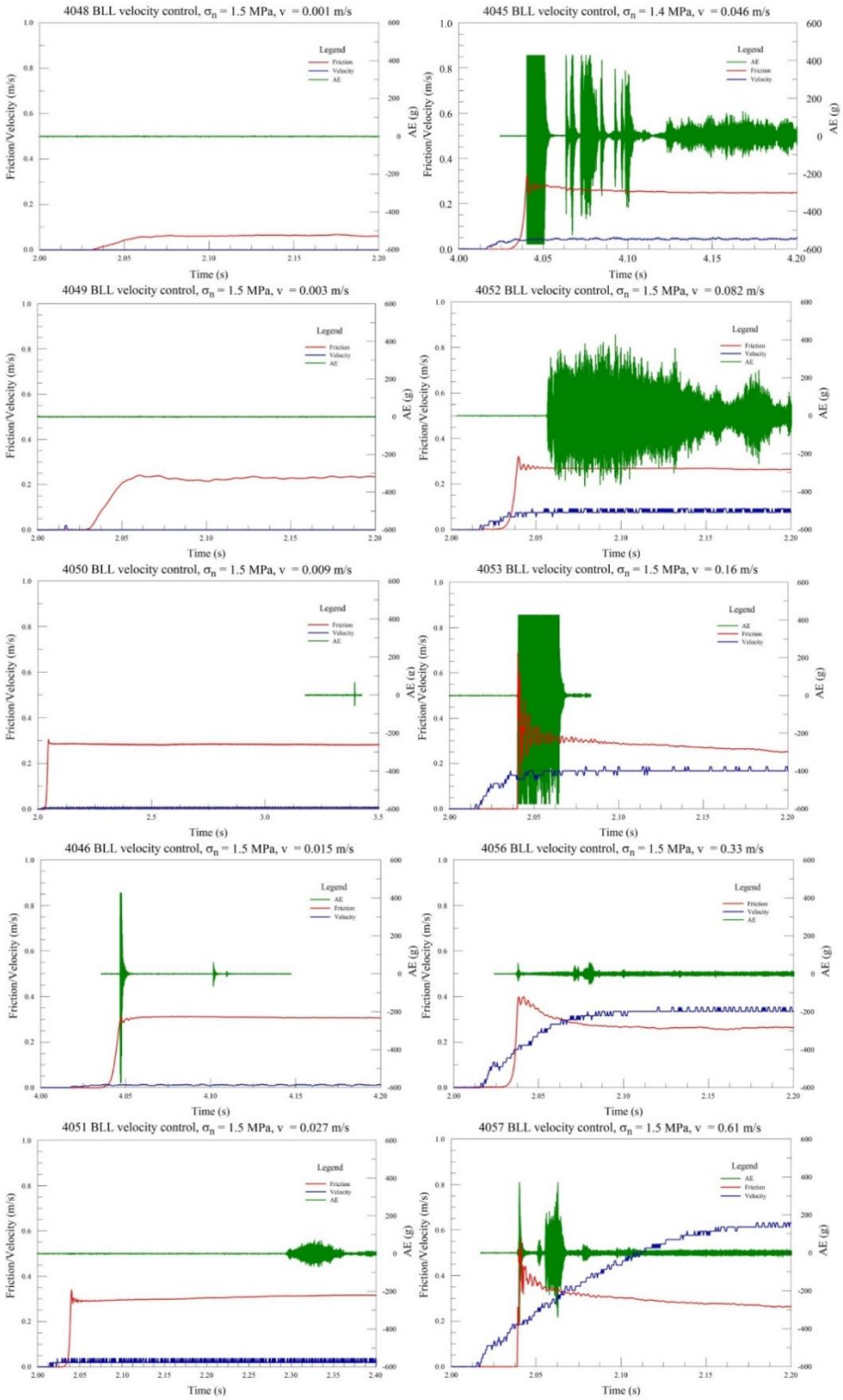

Fig. 4.7 A series of BLL velocity control experiments with initial AE shown with progressively increasing velocity commands (upper left to lower left, then upper right to lower right).

Chapter 5 Discussion and summary

Energy profiles of power-density control experiments

The PD, which is the product of slip-velocity and shear-stress is expected to provide a constant energy rate to the experimental fault without dictating the slip-velocity or the shear stress. This control is realized by a feedback loop on the controlling program that adjusts the motor speed to match the requested PD.

It was noted that under PD control, the experimental fault may move in a jerky mode in response to rock properties and noise of the control program. This spontaneous, self-adaptive behavior might be a realistic simulation of natural earthquakes that do not slip in a time predictable manner. Consider experiment #4045 (Fig. 5.1a) during which a series of three PD levels were requested (green curve). The time integrated PD indicates the requested cumulative energy density (ED) (black curve) throughout the experiment. The dashed blue curve is the actual energy-density, as calculated by integration of the product of measured shear stress and slip-velocity. The curve of actual energy-density (dashed blue) follows the trend of the requested energy-density (black), but with the additional features as follows.

1. The actual energy-density displays a stepping pattern, in which a ramping up stage is a slip event and a flat (or plateau) stage is a ‘stick’ period. This feature reflects the spontaneous occurrence of the stick-slip events under constant PD (Fig. 3.1, 3.4).

2. The actual energy-density (=actual energy dissipation) does not always match the requested one, as manifested by the relative positions of the black and blue curves. During periods of low requested PD, the energy consumption falls behind the energy supply (namely, blue curve being below black curve). During

medium PD, the actual follows the requested fairly closely, and during high requested PD, the actual energy slightly exceeds the requested.

3. At the end of the experiment, there is a slight mismatch between requested and actual energy-densities that is related to both mechanics of the experimental fault and the operating control system.

The energy profiles in Fig. 5.1 reflect the spontaneous response of the experimental fault to a constant requested energy rate (PD). This is interpreted as an analog for a natural tectonic system that applies a semi-constant loading rate on a given fault, which spontaneously moves in a jerky pattern of earthquakes.

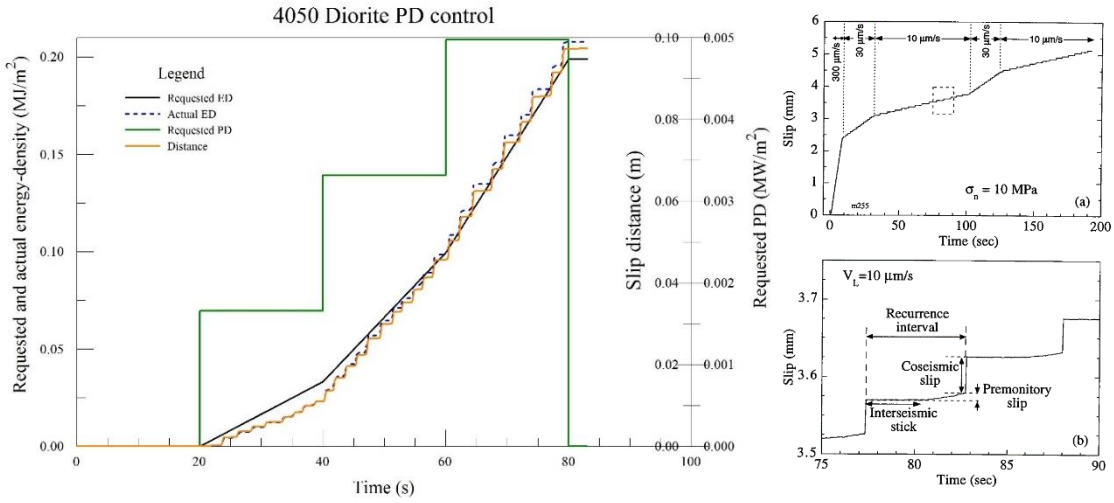

(a) (b)

Fig. 5.1 (a) Energy profiles of PD control experiments. (b) Slip curve of stick-slip indirect shear experiments (Karner and Marone, 2000).

The actual energy curve (dashed blue in Fig. 5.1a) is generally similar to displacement curve in classical stick-slip experiments (e.g. Fig. 5.1b), but they show different properties of the experimental fault, and they are the results of different loading methods. In the case of classical stick-slip experiments, loading is in

displacement-rate (e.g. Fig. 5.1b; Karner and Marone, 2000) or differential stress (e.g., Byerlee and Brace, 1968), while in the case of PD control loading, energy-rate serves as the controlling boundary condition. For comparison, Fig. 5.1a also shows displacement curve in orange, which trends similarly as actual ED. Both actual ED and displacement is comparable to that of stick-slip experiments in direct shear experiments by Karner and Marone (2000) (Fig. 5.1b).

Implications of PD control experiments to natural earthquakes

Here I compare my experimental results to field observation of San Andreas and Calaveras faults in California. Fig. 5.2a shows displacement profiles of CBD experiment #3505. The profile under lower PD is plotted in enlarged scale on creep displacement axis. Displacement curve of the creep event shows an upward concave profile (Fig. 5.2b), and the micro-seismic stick-slip curve is sigmoidal: early concave and late convex profile (Fig. 5.1c). This reflects that the former has lower acceleration then higher, and the latter has the inverse. Creep events have precursory slip (arrow in Fig. 5.2b) prior to the main slip, while micro-seismic stick-slip have no precursors.

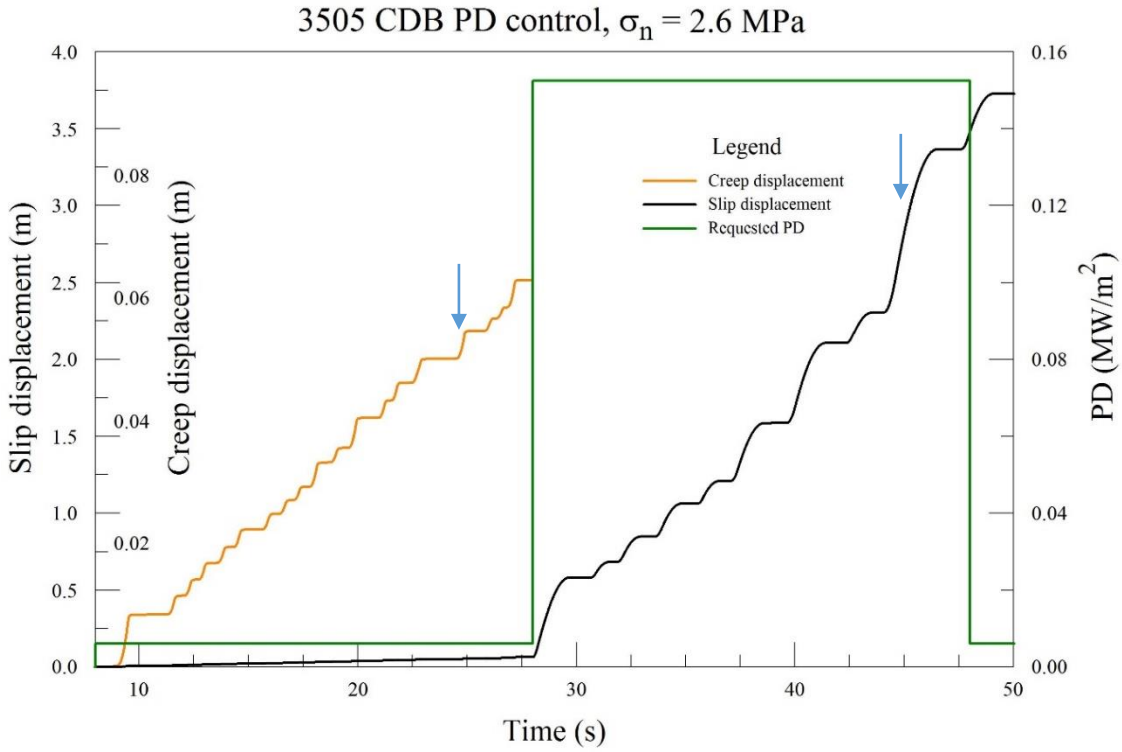

(a)

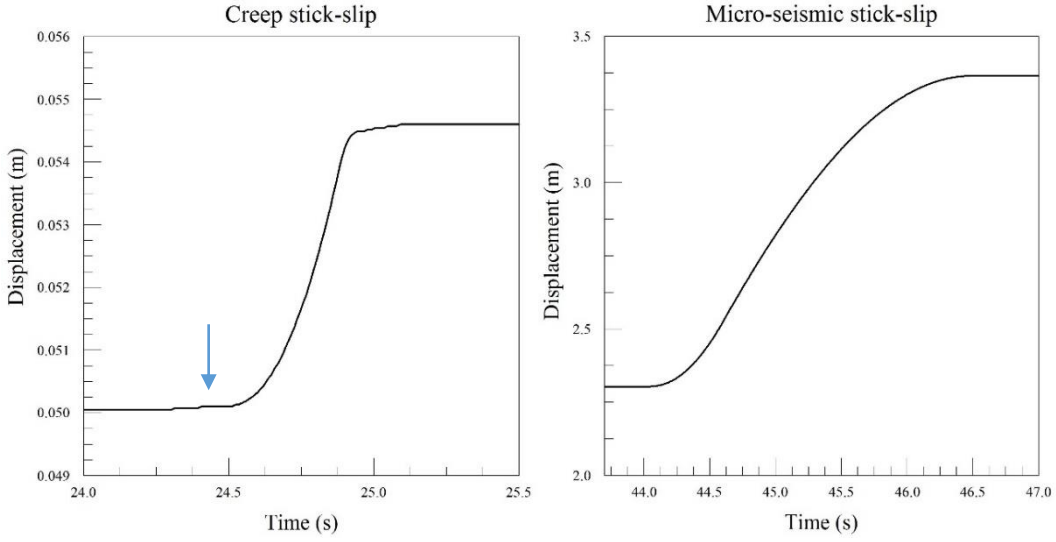

(b) (c)

Fig. 5.2 Displacement profile of (a) a PD control experiment, (b) a creep events event (left arrow on (a)), (c) a micro-seismic stick-slip event (right arrow on (a)).

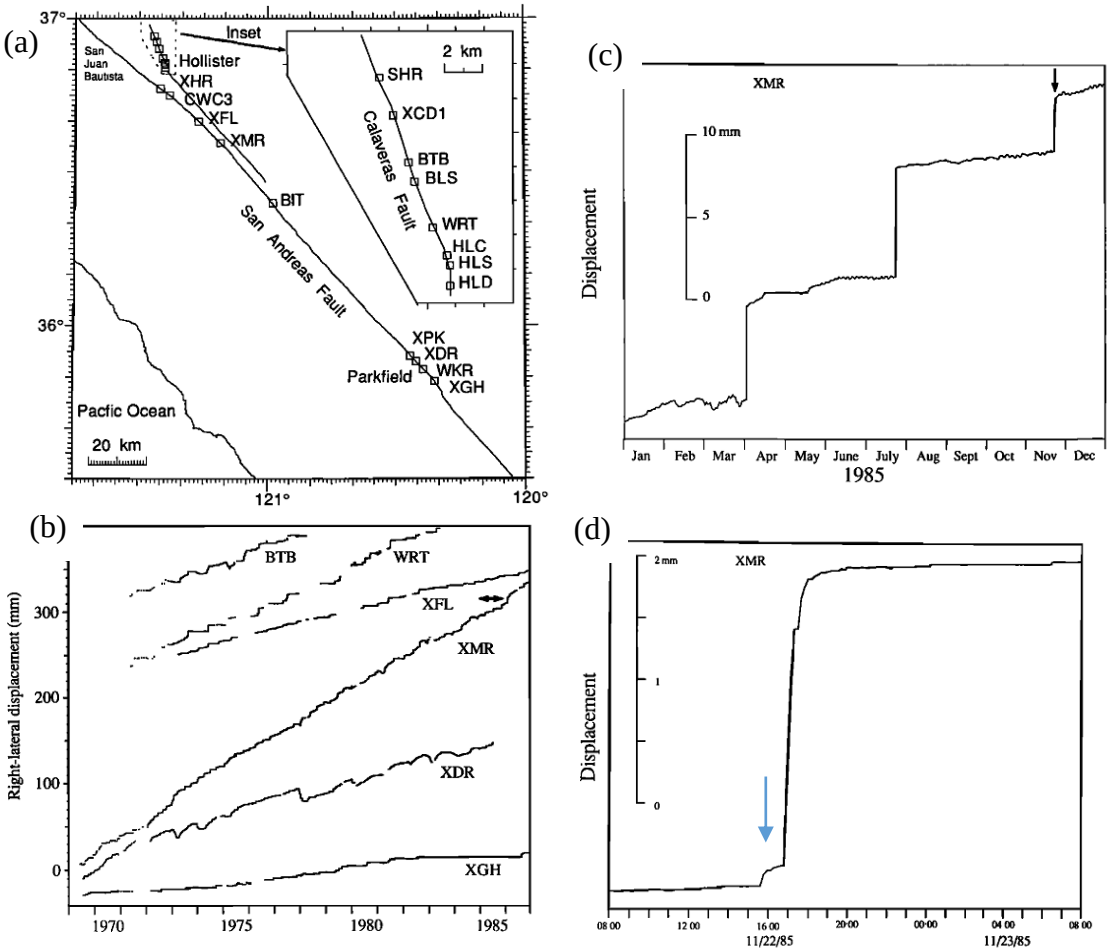

Fig. 5.3 (a) Locations of creepmeters mentioned in this section (Wesson, 1988). (b) Long-term observations from selected creepmeters along the San Andreas and Calaveras faults in California. Note the typical pattern of secular slip and creep events at most stations. For details of the instrumentation and discussion of the data, see Schulz et al. (1982). (c) and (d) Details of the creep observations at XMR during times indicated by the arrows in Figures (b) and (c) (Wesson, 1988).

Fig. 5.3 shows field observation from creepmeters installed across the San Andreas and Calaveras faults, California, with over a decade of monitoring (Schulz et al., 1982; Wesson, 1988). Fig. 5.3c, d show details of the creep observations at XMR site during times indicated by the arrows in Fig. 5.3b, c. One can note that the laboratory creep events (Fig. 5.2a, b) are very similar to the creep events at station XMR on the southern segment of San Andreas Fault (Fig. 5.3c, d). They both have

displacements of a few mm (Fig. 5.2a, Fig. 5.3b), and the occurrence of a precursor prior to the main creep event Fig. 5.2b (arrow) and Fig. 5.3d (arrow).

The experimental micro-seismic stick-slip events under higher PD, show variable average slip rates and up to ~0.5 m displacements. One may speculate that these features are analogous to fault segments experiencing earthquakes, for example on the creeping segment of San Andreas Fault near Parkfield. The creepmeter data at Parkfield vicinity show small displacement episodes that are similar to the present experimental observations. I propose that creep events in the PD experiments are a good proxy for natural creep events, and micro-seismic stick-slip may serve as analog to medium-size earthquakes along the San Andreas Fault.

Summary

This research of fault rupture processes in high-speed rotary shear experiments is composed of two parts. The first part focuses on developing a new, realistic experimental loading method, *power-density control* loading, which could generate stick-slip, the most commonly known model for earthquakes. There are two types of slip-events -- creep events and micro-seismic stick-slip, which occur spontaneously under constant requested energy-rates. These spontaneous events appear as good proxies of earthquakes.

The second part of this study is concerned with acoustic emissions (AEs) during high-speed rotary shear experiments. Four accelerometers are installed near to the experimental fault and could provide crucial information in the form of three-dimensional data. With 3D AEs, I located the sources of AEs and interpreted them as the breakdown of asperities on the experimental fault surface. A tentative map of rupture propagation was obtained with asperities breading down at two major sites.

Additionally, initial AEs in velocity control experiments are mostly concurrent with the peak stress, but extensive work is needed to achieve a robust understanding.

In total, I conducted 76 power-density control experiments and 66 velocity control experiments on various types of rocks including granite, diorite, and limestone, at slip rates approaching seismic slip velocities (~ 1 m/s). Of all the experiments, 70 have AE data available. The results show that power-density control loading with AE recording could give a more realistic simulation of fault rupture with the possibility of rupture visualization.

Future plan of research

Experimental work

I will run a series of new experiments with refined design of accelerometer distribution and with shape-simplified rock samples. Both velocity control and power control experiments are planned. A spectrum of different velocities and powers will be included to obtain a more complete scenario of rock behaviors in terms of stick-slip and rupture propagation. Various rock types will be tested in this framework in order to investigate the lithological dependence on rupture propagation. Bi-material faults will also be assembled for testing.

Analysis

Statistical analysis

With the data from past experiments, I will compile different types of runs into a single database. Systematic analysis of event extraction, seismic parameter calculation, and error correction will be done. Single events will be put into statistical analysis to reveal new possible relations.

Rupture visualization

I will improve the accuracy of source location of AEs and develop easy-to-use software package for rupture visualization. With that established, manual picking of first arrivals will turn into automatic picking, on both acceleration and velocity diagrams.

Spectral analysis

Focus will be drawn to derivation of source parameters of AEs including slip-distance, stress drop, magnitude, energy budget, etc. (Abercrombie, 1995; Brune, 1970). Results will be compared with natural earthquakes to test the suitability of laboratory stick-slip as natural proxy of large earthquakes.

References

Abercrombie, R. E., 1995, Earthquake source scaling relationships from-1 to 5 ML using seismograms recorded at 2.5-km depth: J. geophys. Res, v. 100, no. B2, p. 24015-24036.

Beeler, N. M., Lockner, D. L., and Hickman, S. H., 2001, A simple stick-slip and creep-slip model for repeating earthquakes and its implication for microearthquakes at Parkfield: Bulletin of the Seismological Society of America, v. 91, no. 6, p. 1797-1804.

Brace, W., and Byerlee, J., 1966, Stick-slip as a mechanism for earthquakes: Science, v. 153, no. 3739, p. 990-992.

Brune, J. N., 1970, Tectonic stress and the spectra of seismic shear waves from earthquakes: Journal of geophysical research, v. 75, no. 26, p. 4997-5009.

Byerlee, J. D., and Brace, W. F., 1968, Stick Slip Stable Sliding and Earthquakes: Transactions-American Geophysical Union, v. 49, no. 1, p. 300-&.

Carpenter, B. M., Marone, C., and Saffer, D. M., 2011, Weakness of the San Andreas Fault revealed by samples from the active fault zone: Nature Geoscience, v. 4, no. 4, p. 251-254.

Chang, J. C., Lockner, D. A., and Reches, Z., 2012, Rapid acceleration leads to rapid weakening in earthquake-like laboratory experiments: Science, v. 338, no. 6103, p. 101-105.

Chen, X. F., Madden, A. S., Bickmore, B. R., and Reches, Z., 2013, Dynamic weakening by nanoscale smoothing during high-velocity fault slip: Geology, v. 41, no. 7, p. 739-742.

Di Toro, G., Goldsby, D. L., and Tullis, T. E., 2004, Friction falls towards zero in quartz rock as slip velocity approaches seismic rates: Nature, v. 427, no. 6973, p. 436-439.

Di Toro, G., Han, R., Hirose, T., De Paola, N., Nielsen, S., Mizoguchi, K., Ferri, F., Cocco, M., and Shimamoto, T., 2011, Fault lubrication during earthquakes: Nature, v. 471, no. 7339, p. 494-498.

Dieterich, J. H., 1978, Time-Dependent Friction and Mechanics of Stick-Slip: Pure and Applied Geophysics, v. 116, no. 4-5, p. 790-806.

Dieterich, J. H., and Kilgore, B. D., 1994, Direct observation of frictional contacts: New insights for state-dependent properties: Pure and Applied Geophysics, v. 143, no. 1-3, p. 283-302.

Kanamori, H., and Brodsky, E. E., 2004, The physics of earthquakes: Reports on Progress in Physics, v. 67, no. 8, p. 1429.

Karner, S. L., and Marone, C., 2000, Effects of Loading Rate and Normal Stress on Stress Drop and Stick-Slip Recurrence Interval: GeoComplexity and the Physics of Earthquakes, p. 187-198.

Liao, Z., and Reches, Z. e., 2013, Modeling Dynamic-Weakening and Dynamic-Strengthening of Granite in High-Velocity Slip Experiments, INTECH Open Access Publisher.

Liao, Z. H., Chang, J. C., and Reches, Z., 2014, Fault strength evolution during high velocity friction experiments with slip-pulse and constant-velocity loading: Earth and Planetary Science Letters, v. 406, p. 93-101.

Lockner, D. A., Morrow, C., Moore, D., and Hickman, S., 2011, Low strength of deep San Andreas fault gouge from SAFOD core: Nature, v. 472, no. 7341, p. 82-85.

Lockner, D. A., and Okubo, P. G., 1983a, Measurements of frictional heating in granite: Journal of Geophysical Research: Solid Earth (1978–2012), v. 88, no. B5, p. 4313-4320.

Marone, C., 1998, Laboratory-derived friction laws and their application to seismic faulting: Annual Review of Earth and Planetary Sciences, v. 26, p. 643-696.

McLaskey, G. C., and Glaser, S. D., 2011, Micromechanics of asperity rupture during laboratory stick slip experiments: Geophysical Research Letters, v. 38, no. 12, p. n/a-n/a.

McLaskey, G. C., Lockner, D. A., Kilgore, B. D., and Beeler, N. M., 2015, A Robust Calibration Technique for Acoustic Emission Systems Based on Momentum Transfer from a Ball Drop: Bulletin of the Seismological Society of America, v. 105, no. 1, p. 257-271.

Nielsen, S., Taddeucci, J., and Vinciguerra, S., 2010, Experimental observation of stick-slip instability fronts: Geophysical Journal International, v. 180, no. 2, p. 697-702.

Niemeijer, A., Di Toro, G., Nielsen, S., and Di Felice, F., 2011, Frictional melting of gabbro under extreme experimental conditions of normal stress, acceleration, and sliding velocity: Journal of Geophysical Research: Solid Earth (1978–2012), v. 116, no. B7.

Ohnaka, M., Kuwahara, Y., and Yamamoto, K., 1987, Constitutive relations between dynamic physical parameters near a tip of the propagating slip zone during stick-slip shear failure: Tectonophysics, v. 144, no. 1, p. 109-125.

Ohnaka, M., and Yamashita, T., 1989, A cohesive zone model for dynamic shear faulting based on experimentally inferred constitutive relation and strong motion source parameters: Journal of Geophysical Research: Solid Earth, v. 94, no. B4, p. 4089-4104.

Okubo, P. G., and Dieterich, J. H., 1981, Fracture energy of stick-slip events in a large scale biaxial experiment: Geophysical Research Letters, v. 8, no. 8, p. 887-890.

Percival, D. B., and Walden, A. T., 1993, Spectral analysis for physical applications, Cambridge University Press.

Reches, Z., and Lockner, D. A., 2010, Fault weakening and earthquake instability by powder lubrication: Nature, v. 467, no. 7314, p. 452-U102.

Rubinstein, S. M., Barel, I., Reches, Z. e., Braun, O. M., Urbakh, M., and Fineberg, J., 2011, Slip Sequences in Laboratory Experiments Resulting from Inhomogeneous Shear as Analogs of Earthquakes Associated with a Fault Edge: Pure and Applied Geophysics, v. 168, no. 12, p. 2151-2166.

Schulz, S. S., Mavko, G. M., Burford, R. O., and Stuart, W. D., 1982, Long-term fault creep observations in central California: Journal of Geophysical Research: Solid Earth, v. 87, no. B8, p. 6977-6982.

Shimamoto, T., and Tsutsumi, A., 1994, A new rotary-shear high-speed frictional testing machine: its basic design and scope of research: J. Tecton. Res. Group Jpn, v. 39, p. 65-78.

Sone, H., and Shimamoto, T., 2009, Frictional resistance of faults during accelerating and decelerating earthquake slip: Nature Geoscience, v. 2, no. 10, p. 705-708.

Tullis, T. E., and Weeks, J. D., 1987, Constitutive behavior and stability of frictional sliding of granite, Friction and faulting, Springer, p. 383-414.

Wesson, R. L., 1988, Dynamics of fault creep: Journal of Geophysical Research: Solid Earth, v. 93, no. B8, p. 8929-8951.

Zoback, M. D., Zoback, M. L., Mount, V. S., Suppe, J., Eaton, J. P., Healy, J. H., Oppenheimer, D., Reasenberg, P., Jones, L., and Raleigh, C. B., 1987, New evidence on the state of stress of the San Andreas fault system: Science, v. 238, no. 4830, p. 1105-1111.

Appendix A: Table of PD control experiments in this study

Exp #	Sample	Requested PD (MW/m2)			Stick-slip occurrence			Sampling rate (Hz)	σn (MPa)	Max V (m/s)	D (m)	μmax	Max T (°C)	AE data
		Level 1	Level 2	Level 3	Level 1	Level 2	Level 3							
3385	RRG	N/A			N/A			64	2.18	0.02	0.07	0.57	24	No
3386	RRG	N/A			N/A			16	2.20	0.42	0.85	0.57	24	No
3387	RRG	N/A			N/A			64	2.20	0.08	0.42	0.59	28	No
3388	RRG	N/A			N/A			16	2.20	0.01	0.20	0.60	26	No
3389	RRG	N/A			N/A			16	2.21	0.05	1.23	0.65	39	No
3410	RRG	N/A			N/A			16	2.16	0.02	0.45	0.62	23	No
3411	RRG	N/A			N/A			64	1.34	0.04	0.31	0.86	29	No
3412	RRG	N/A			N/A			64	1.34	0.02	0.28	0.80	26	No
3413	RRG	N/A			N/A			64	1.34	0.08	0.56	0.90	32	No
3425	RRG	N/A			N/A			64	2.14	0.08	0.30	0.68	32	No
3426	RRG	N/A			N/A			16	2.14	0.08	1.20	0.65	39	No
3427	RRG	N/A			N/A			32	2.15	0.09	1.07	0.69	39	No
3428	RRG	N/A			N/A			16	2.16	0.11	3.98	0.68	54	No
3430	RRG	0.0087	0.00943		Yes	Yes		64	2.14	0.01	0.01	0.77	22	No
3431	RRG	0.0622			Yes			64	3.51	0.30	0.88	0.72	55	No
3432	RRG	0.0622			Yes			64	2.17	0.33	1.36	0.83	47	No
3433	RRG	0.0057	0.06218		Yes	Yes		16	2.19	0.45	1.74	0.81	62	No
3434	RRG	0.0058	0.06234		Yes	Yes		64	3.53	0.28	0.92	0.75	35	No
3435	RRG	0.0058	0.06223		Yes	Yes		256	2.18	0.31	1.54	0.87	63	No
3436	RRG	0.0057	0.06227		Yes	Yes		256	2.18	0.32	1.53	0.86	43	No
3437	RRG	0.0058	0.06231		Yes	Yes		10	2.18	0.39	1.24	0.84	50	No
3438	RRG	0.0057	0.06222		No	Yes		10	3.53	0.28	0.66	0.78	40	No
3439	RRG	0.0057	0.0622		No	Yes		10	3.55	0.33	2.28	0.72	64	No
3440	RRG	N/A			N/A			10	N/A	N/A	N/A	N/A	N/A	No
3441	RRG	N/A			N/A			64	3.56	0.02	0.06	0.50	23	No
3442	RRG	N/A			N/A			256	3.56	0.03	0.08	0.50	24	No
3443	RRG	N/A			N/A			32	2.20	0.05	0.06	0.50	24	No
3445	RRG	N/A			N/A			32	2.04	0.05	1.59	0.73	39	No
3446	RRG	0.0048	0.02633		Yes	Yes		128	3.39	0.16	2.55	0.66	37	No
3447	RRG	0.0059	0.00809	0.04094	No	No	N/A	32	3.39	0.14	2.64	0.40	37	No
3448	RRG	0.0059	0.0081	0.04098	No	No	No	32	3.39	0.11	2.74	0.74	41	No
3449	RRG	0.0044	0.00446		Yes	Yes		32	3.38	0.01	0.04	0.51	26	No
3450	RRG	0.0117			Yes			128	3.38	0.37	1.43	0.87	47	No
3451	RRG	N/A			N/A			100	2.07	0.01	0.01	0.68	26	No
3452	RRG	0.0045			Yes			128	3.37	0.01	0.00	0.67	24	No
3453	RRG	N/A			N/A			128	3.39	0.66	1.38	0.83	43	No
3455	RRG	0.0052	0.01171		No	No		128	3.40	0.02	0.18	0.68	25	No

***AE data: No means none available, 1 or 4 means 1 or 4 accelerometer(s).**

Exp #	Sample	Requested PD (MW/m2)			Stick-slip occurrence			Sampling rate (Hz)	σn (MPa)	Max V (m/s)	D (m)	μmax	Max T (°C)	AE data
		Level 1	Level 2	Level 3	Level 1	Level 2	Level 3							
3456	RRG	0.0051	0.00659	0.0117	Yes	Yes	N/A	128	3.40	0.02	0.03	0.68	21	No
3457	RRG	0.0051	0.00659	0.0117	No	No	Yes	64	2.09	0.11	0.19	0.64	24	No
3461	CBD	0.0063	0.00641	0.00653	No	Yes	Yes	128	3.21	0.00	0.03	0.69	20	No
3462	CBD	N/A			N/A			128	3.13	0.00	0.01	0.73	23	No
3463	CBD	0.0066	0.00696		Yes	Yes		128	3.23	0.00	0.02	0.59	22	No
3464	CBD	0.0066	0.01022		Yes	Yes		128	3.18	0.02	0.04	0.59	22	No
3465	CBD	0.0065	0.01019		Yes	Yes		128	3.19	0.02	0.04	0.73	22	No
3466	CBD	N/A			N/A			128	N/A	N/A	N/A	N/A	N/A	No
3467	CBD	0.0068	0.01061		Yes	Yes		128	2.76	0.03	0.05	0.76	23	No
3480	CBD	0.0069	0.01075		Yes	Yes		128	2.61	0.02	0.05	0.69	23	No
3481	CBD	0.0108	0.015	0.01926	Yes	Yes	Yes	256	2.63	0.22	1.12	0.79	61	No
3482	CBD	N/A			N/A			256	2.62	0.07	0.02	0.69	20	No
3483	CBD	N/A			N/A			256	2.59	0.07	0.02	0.61	20	No
3484	CBD	N/A			N/A			256	2.60	0.13	0.07	0.72	22	No
3485	CBD	N/A			N/A			256	2.61	0.15	0.07	0.70	24	No
3486	CBD	N/A			N/A			256	2.64	0.11	0.04	0.72	22	No
3487	CBD	N/A			N/A			256	2.64	0.16	0.07	0.78	25	No
3488	CBD	N/A			N/A			256	2.66	0.15	0.29	0.68	30	No
3489	CBD	N/A			N/A			256	2.64	0.14	0.25	0.74	31	No
3490	CBD	0.0086	0.02772		Yes	Yes		256	2.64	0.21	0.92	0.72	53	No
3500	CBD	0.0093	0.0478		Yes	Yes		256	2.64	0.12	0.56	0.72	43	No
3501	CBD	0.0092	0.0475		Yes	Yes		256	2.65	0.13	0.60	0.71	47	No
3502	CBD	0.0002			Yes			128	2.56	0.01	0.06	0.84	23	No
3503	CBD	0.0094			Yes			128	2.58	0.04	0.38	0.86	28	No
3504	CBD	0.102			Yes			128	2.58	0.23	2.46	0.92	78	No
3505	CBD	0.0034	0.1693		Yes	Yes		256	2.51	0.80	3.73	1.60	111	No
4041	CBD	0.005	0.1775		N/A	N/A		256	2.16	0.75	0.47	2.93	22	No
4042	CBD	0.0167			N/A			256	2.36	1.56	3.33	4.15	34	No
4043	CBD	0.0154			Yes			128	2.26	0.05	0.15	0.57	28	1
4044	CBD	0.0154			Yes			128	2.22	0.04	0.13	0.96	24	1
4045	CBD	0.0097			Yes			128	3.22	0.22	0.29	0.74	26	4
4046	CBD	0.0088			N/A			128	3.31	1.66	5.48	0.92	103	4
4047	CBD	0.0089			N/A			128	3.31	0.85	1.34	0.77	48	4
4048	CBD	0.0065	0.00687	0.00727	Yes	Yes	Yes	128	3.33	0.00	0.01	0.78	23	4
4049	CBD	0.0065	0.00687	0.00727	Yes	Yes	Yes	128	3.39	0.01	0.01	0.68	20	4
4050	CBD	0.0073	0.00848	0.00968	Yes	Yes	Yes	128	3.34	0.02	0.10	0.70	21	4
4051	CBD	-1E-03	0.153		Yes	Yes		256	2.65	0.127	0.6	0.71	47	No
4052	CBD	-1E-03	0.1536		N/A	N/A		256	2.563	0.006	0.06	0.84	23	No
4053	CBD	-9E-04	0.154		N/A	N/A		128	2.575	0.0395	0.38	0.86	28	No

Appendix B: Documentation of MATLAB programs for this research

Accel_v1

Accel_v1 is a MATLAB program for analyzing data from experiments on ROGA system, with a highlight of analyzing acoustic emission data from accelerometers. Functions (buttons) are summarized as follows (Fig. A1).

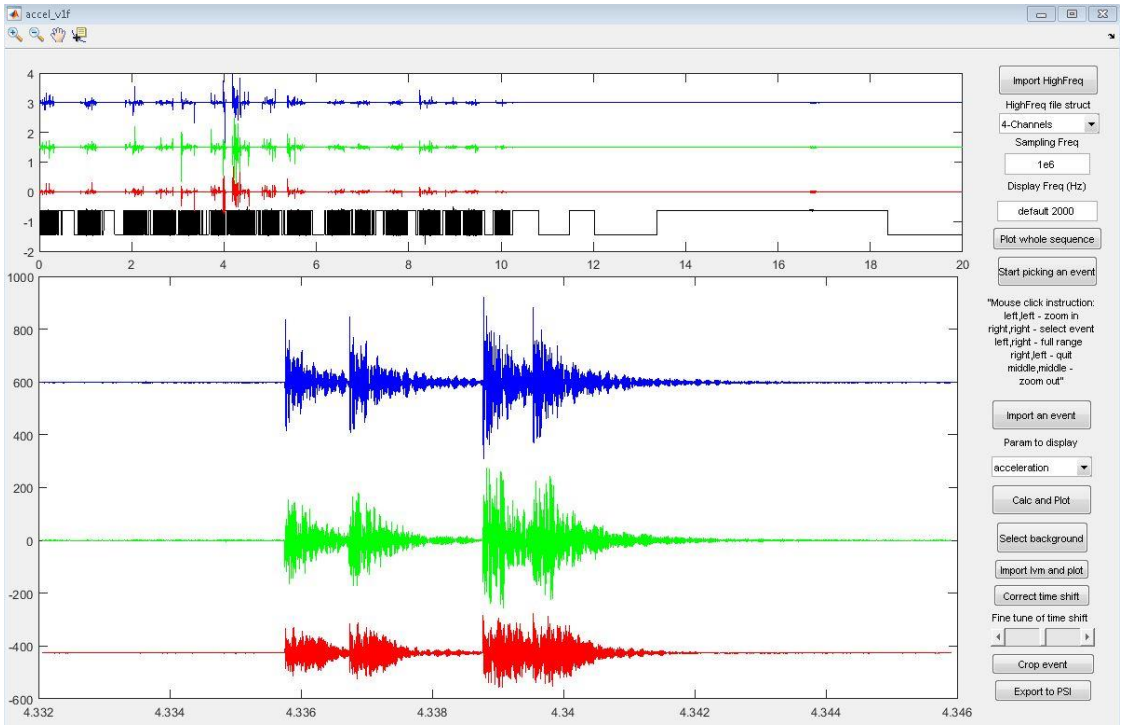

Fig. A1 Screenshot of Accel_v1

Import HighFreq: import high frequency data file (*.txt or *.*).

HighFreq file struct: select whether the high frequency file is a 4 channel structure or 8 channel structure.

Sampling Freq: type in sampling frequency of the high frequency recording.

Display Freq (Hz): frequency for down-sampling the high frequency data for the convenience of plotting whole sequence. Using default value works well.

Plot whole sequence: plot whole sequence of AE data with encoder volts in black.

Start picking an event: pick the start and end of an AE event with instructions shown below the button.

Import an event: import a previously stored AE event (MAT-file).

Param to display: choose acceleration, velocity, or displacement to display for 3 channels.

Calc and Plot: calculate full time series of the selected or imported event and plot.

Select background: select a start and an end of background level for demeaning purposes. Remember to Calc and Plot after selection.

Import lvm and plot: import low frequency file for synchronization (aligning encoder). Remember to import *.lvm file not c40 file.

Correct time shift: begin aligning encoder.

Fine tune of time shift: for fine adjustment of encoder alignment.

Crop event: for trimming an event so that the first arrival is near zero time and coda is removed.

Export PSI: export the selected event to ASCII file for import to PSI software. The file has time, acceleration, velocity and displacement in it.

Accel_v2

Accel_v2 is an updated version of Accel_v1 with additional capability of hypocenter locating and performance improvement. The functions (buttons) are described as follows (Fig. A2).

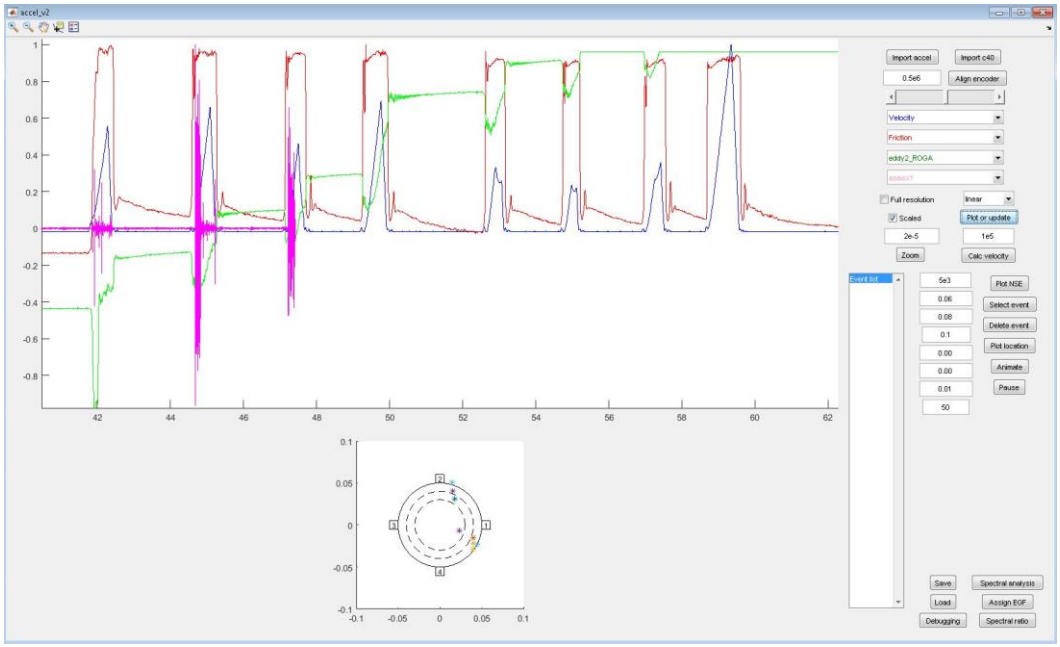

Fig. A2a Screenshot of Accel_v2. Plots of mechanical parameters and hypocenter locations.

Import accel: select one of the accel files (*.txt, *. *) of the four accelerometer data and the program will automatically recognize the others.

Import c40: select c40 file of low frequency recording.

Align encoder: after typing in the sampling frequency to the left of Align encoder button, this button imports all the AE data and low frequency data and plot them in the two windows and enters a sync mode to align encoder. After selecting corresponding positions, the encoder can be fine-tuned with the slider below the button.

Drop-down menus: select parameters to display.

Full resolution: for AE data, full resolution slows the display, but is required when picking first arrivals. Click Plot or update after change.

Scaled: scale all the parameters shown in the window so that they can all stretch to the window height. Click Plot or update after change.

Plot or update: plot curves or update curves in the window.

Zoom: enters a zoom and pan mode for displaying purposes.

Calc velocity: calculates velocity based on encoder of high frequency channels. The text boxes above the button are velocity calculation window width and encoder step length respectively.

Listbox: shows picked AE events.

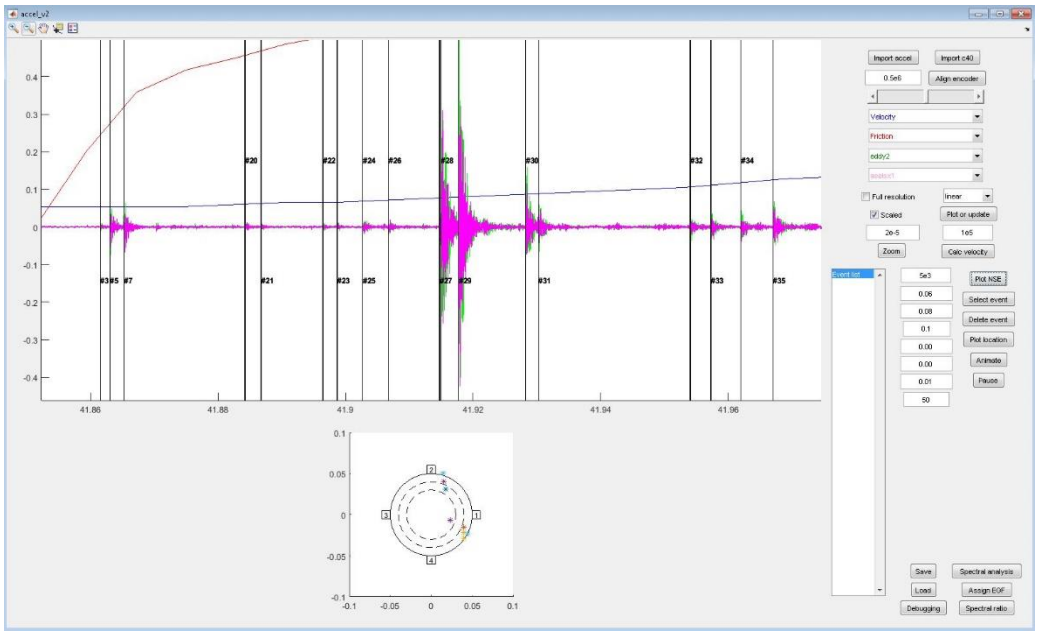

Fig. A2b Screenshot of Accel_v2. Accelerograms with AE event labels and hypocenter locations.

Plot NSE: labels AE positions on accelerograms.

Select event: select AE events (start and end).

Delete event: delete AE events in the listbox.

Plot location: calculate hypocenter locations and plot them on the sample surface in the lower window.

Animate: show an animation of AE occurrence through time.

Pause: pause the animation.

Textboxes: hover on the boxes to see parameter names and change accordingly.

Save: save the data and events to the workspace of MATLAB.

Load: load from workspace.

Debugging: enters a debug mode.

Spectral analysis, Assign EGF, Spectral ratio: reserved for spectral analysis tools.

Appendix C: List of Symbols

PD: Power-density

ED: Energy-density

σn: Normal stress

τ: Shear stress

μ: Coefficient of friction defined as shear stress divided by normal stress (τ/σn)

D: Experimental slip distance/displacement

V: Experimental linear slip-velocity of samples

RRG: Radiant Red Granite

CBD: Charcoal Black Diorite

BLL: Brown Lueders Limestone

PID: Proportional–integral–derivative

AE: Acoustic emission